The Astrophysical Journal, 931:154 (19pp), 2022 June 1 https://doi.org/10.3847/1538-4357/ac6a5d

Exploring Changes in Quasar Spectral Energy Distributions across C IV Parameter Space

Angelica B. Rivera[1], Gordon T. Richards[2], Sarah C. Gallagher[3,4], Trevor V. McCaffrey[2], Amy L. Rankine[5], Paul C. Hewett[6], and Ohad Shemmer[7]

[1] Department of Physics, United States Naval Academy, 572C Holloway Rd., Annapolis, MD 21402, USA; arivera@usna.edu
[2] Department of Physics, Drexel University, 32 S. 32nd Street, Philadelphia, PA 19104, USA
[3] Department of Physics and Astronomy, Western University, 1151 Richmond St., London, ON N6C 1T7, Canada
[4] The Institute for Earth and Space Exploration, Western University, 1151 Richmond St., London, ON N6C 1T7, Canada
[5] Institute for Astronomy, University of Edinburgh, Royal Observatory, Edinburgh, EH9 3HJ, UK
[6] Institute of Astronomy, University of Cambridge, Madingley Road, Cambridge, CB3 0HA, UK
[7] Department of Physics, University of North Texas, Denton, TX 76203, USA
Received 2021 September 24; revised 2022 April 16; accepted 2022 April 20; published 2022 June 6

Abstract

We examine the UV/X-ray properties of 1378 quasars in order to link empirical correlations to theoretical models of the physical mechanisms dominating quasars as a function of mass and accretion rate. The clarity of these correlations is improved when (1) using C IV broad emission line equivalent width (EQW) and blueshift (relative to systemic) values calculated from high signal-to-noise ratio reconstructions of optical/UV spectra and (2) removing quasars expected to be absorbed based on their UV/X-ray spectral slopes. In addition to using the traditional C IV parameter space measures of C IV EQW and blueshift, we define a "C IV $\|$ distance" along a best-fit polynomial curve that incorporates information from both C IV parameters. We find that the C IV $\|$ distance is linearly correlated with both the optical-to-X-ray slope, $\alpha_{\rm ox}$, and broad-line He II EQW, which are known spectral energy distribution indicators, but does not require X-ray or high spectral resolution UV observations to compute. The C IV $\|$ distance may be a better indicator of the mass-weighted accretion rate, parameterized by $L/L_{\rm Edd}$, than the C IV EQW or blueshift alone, as those relationships are known to break down at the extrema. Conversely, there is only a weak correlation with the X-ray energy index (Γ), an alternate $L/L_{\rm Edd}$ indicator. We find no X-ray or optical trends in the direction perpendicular to the C IV distance that could be used to reveal differences in accretion disk, wind, or corona structure that could be widening the C IV EQW–blueshift distribution. A different parameter (such as metallicity) not traced by these data must come into play.

Unified Astronomy Thesaurus concepts: Quasars (1319); Spectral energy distribution (2129); Black hole physics (159); X-ray active galactic nuclei (2035)

Supporting material: data behind figure

1. Introduction

A long-standing goal in the studies of active galactic nucleus (AGN) physics is to be able to classify quasars based on their fundamental physical properties, such as accretion rate, mass, and spin, together with viewing angle. However, these properties are currently difficult to measure accurately for large samples of quasars. Alternately, empirical parameter spaces such as the Hβ "Eigenvector 1" parameter space at low redshift (EV1; Boroson & Green 1992; Shen & Ho 2014; Marziani et al. 2018) and the C IV parameter space (C IV equivalent width (EQW), FWHM, and "blueshift" of the emission-line peak relative to systemic; Sulentic et al. 2007; Richards et al. 2011) at high redshift are extremely valuable for identifying gradients in black hole mass and accretion rate. In the case of the C IV parameter space, several questions remain open: is there another main driver behind a quasar's location in these spaces, and do the empirically measured parameters linearly track the underlying physical parameters? Similar to previous investigations (e.g., Brotherton & Francis 1999; Sulentic et al. 2007; Kruczek et al. 2011; Rankine et al. 2020; Timlin et al. 2021a), we seek to investigate these questions by examining the relationships between C IV emission and X-ray properties and spectral energy distribution (SED) indicators. We aim to improve on past work by (1) using the larger amount of (unbiased) data now available, particularly in the multiwavelength archives covering the Sloan Digital Sky Survey (SDSS; York et al. 2000), Chandra (Evans et al. 2010), and XMM-Newton (Jansen et al. 2001); (2) taking advantage of the independent component analysis (Allen et al. 2013; Rankine et al. 2020) technique to reconstruct the ultraviolet (UV) spectra with higher signal-to-noise ratio (S/N) to provide more accurate measurements of emission-line EQWs and blueshifts; (3) using two new C IV parameters (the C IV $\|$ and C IV $\perp$ distances) that incorporate information from both the C IV EQW and blueshift to address the problem of nonlinearity inherent to each parameter alone; and (4) using optical and X-ray data that have first been subject to quality cuts (e.g., Lusso & Risaliti 2016; Timlin et al. 2020a; Pu et al. 2020).

It is important to examine X-ray properties in relation to the C IV parameters because there is a known relationship between the UV and X-ray emission in quasars. There is observational evidence in support of a three-component model of a quasar's UV−X-ray SED. One component is a disk that gives off UV emission as a color−temperature corrected blackbody. This disk gives off some emission in the soft X-ray, but not enough to explain the so-called soft X-ray excess (the second component; Done et al. 2012), which can instead be modeled as emerging from gravitational energy driving optically thick Comptonized disk emission at inner radii. Compton upscattering of disk photons in the X-ray corona forms a power-law tail at hard (>2 keV) X-ray energies, composing the final component.

In a disk plus wind model (e.g., Collin et al. 2006; Czerny & Hryniewicz 2011) of the broad emission line region (BELR), UV photons drive the gas through radiation-line pressure, and X-rays work to undermine the process, stripping the gas of outer-shell electrons (and thus reducing the UV opacity) before the UV photons are able to drive a wind (Murray et al. 1995). As illustrated by Giustini & Proga (2019), whether the wind or disk dominates the broad-line region properties is determined by both the quasar's black hole mass and its accretion rate, with quasars possessing low $L/L_{\rm Edd}$ ($\propto \dot{M}/M$) being the most heavily disk dominated with a "failed wind" consisting of overionized gas, and quasars with high $L/L_{\rm Edd}$ being the most heavily wind dominated (with each type of wind shown by blue stream lines in their Figure 1).

Previous investigations (e.g., Shemmer et al. 2006, 2008; Constantin et al. 2009; Risaliti et al. 2009; Brightman et al. 2013) have found the X-ray photon index, $\Gamma_{\rm hard}$ ($\geqslant$2 keV), to be correlated with $L/L_{\rm Edd}$, but see Trakhtenbrot et al. (2017) for evidence that Γ may only weakly correlate with $L/L_{\rm Edd}$.[8] Γ is given as

$$f_E = N_{\rm 1keV}E^{-\Gamma}({\rm photons/cm^2/s/keV}), \tag{1}$$

where f_E is the flux at a particular energy, $N_{\rm 1keV}$ is the 1 keV normalization constant, and E is the energy. For radio-quiet quasars, Γ averages ∼1.8–2 (George et al. 2000; Reeves & Turner 2000). Γ is related to the X-ray spectral index as $\Gamma = 1\text{–}\alpha_x$ such that larger (more negative) values of Γ (α_x) correspond to a softer SED (Richards et al. 2006) and a quasar expected to have stronger accretion disk winds. It is important to note, however, that there are different ways of calculating Γ, several of which are more reliable than others. While we seek to establish trends between the X-ray and UV properties of the largest sample of quasars possible, we caution that the Γ values utilized within are not the most reliable, and therefore that correlations with Γ may appear weaker than they would otherwise (see Section 3.3 for more discussion on this issue).

With regard to their UV properties, quasars at higher $L/L_{\rm Edd}$ are observed to have low C IV EQWs and high C IV blueshifts (Wang et al. 2011; Shemmer & Lieber 2015; Rankine et al. 2020). However, while the extremes of accretion rate are readily identifiable within the C IV parameter space, intermediate populations are less easily separated. In Rivera et al. (2020) a best-fit curve to the C IV parameter space was utilized in order to group quasars by a "C IV distance" measured from each data point to the top left point on the curve. We similarly use this distance here, as quasars at high mass and low accretion rate and quasars at moderate mass and high accretion rate might have the same C IV distance but could possess different geometries, possibly resulting in different Γ values. These differences may arise, as the X-ray corona is expected to be relatively stronger at lower accretion rates (Giustini & Proga 2019). In recognition of the results of Rankine et al. (2020) with regard to He II EQW as a metric of ionization, we additionally define a C IV "perpendicular distance" that describes the distance from the nearest point on the best-fit curve—in order to seek trends with the parameter that causes the "scatter" from that curve. We seek to examine the trends between C IV and X-ray properties in order to ascertain whether the Giustini & Proga (2019) model is consistent with the empirical evidence from the UV and X-ray properties considered in tandem.

The format of our paper is as follows: In Section 2, we describe the data we obtained from the literature and the selection and observation of our Chandra/Hubble Space Telescope (HST) targets. In Section 3, we define the X-ray and UV properties that we investigate and our attempts to clean the data of effects such as variability, reddening, and absorption. In Section 4, we address the trends in our subsamples at constant L and z, as well as a method of constraining scatter in the $\alpha_{\rm ox}$–$L_{\rm UV}$ relationship and the implications this has for performing cosmology with quasars. Additionally, in Sections 4.3 and 4.4, we describe the SED indicators used in this paper and how their changes across the C IV parameter space can inform us about physical models, respectively. We conclude in Section 5. Due to the small sample size relative to our whole sample (25 and 1378 quasars, respectively), we describe the reduction of data for our Chandra/HST targets in Appendices A and B. In this work, we assume a flat λCDM cosmology with $h_0 = 67.8$ km s^{-1} Mpc^{-1} and $\Omega_M = 0.308$ (Planck Collaboration et al. 2016).

2. Data

Our goal is to obtain the largest sample possible of high-quality X-ray and UV spectral data of quasars to enable a robust analysis of these properties in tandem. This construction requires incorporating several X-ray and/or UV catalogs from the literature, as well as new observations to fill in gaps in previous sample selections that could bias our results. The majority of our sample is drawn from archival X-ray observations of quasars from SDSS (York et al. 2000), specifically Data Release 14 (Pâris et al. 2014). Timlin et al. (2020a) use X-ray data from the Chandra archives, while Lusso et al. (2020) use data from the SDSS-4XMM catalog (Webb et al. 2020), and these two investigations are largely complementary to each other. The union of these two data sets provides the foundation for our investigation. These data are described in detail in Section 2.1. We additionally include a subsample of multiepoch data from the SDSS-RM sample in Section 2.2 and new Chandra/HST data described in Section 2.3 to construct our full sample. Broad absorption line (BAL; Weymann et al. 1991) and radio-loud (RL) quasars (defined as having $R > 10$, where $R = f_{\rm 6cm}/f_{2500\,\text{Å}}$) are excluded from the Lusso et al. (2020) sample, the Timlin et al. (2020a) sensitive sample, and the Chandra/HST sample because the former are known to be absorbed in X-rays and the latter can have jet-enhanced X-ray emission (Miller et al. 2011; Timlin et al. 2021b).

We further supplement these X-ray data by matching the sources from all four subsamples to those investigated in Rankine et al. (2020), which provides robust and uniform measurement of C IV EQW and C IV blueshift in addition to He II EQW. In all, there are 1378 sources in our investigation with optical/UV spectral coverage of the C IV emission line,

[8] However, while that sample spans the full range of $L/L_{\rm Edd}$, the difference in z between their sample and those at higher redshift (as in our sample) likely means they are sampling a different part of the parameter space illustrated by Figures 1 and 2 in Giustini & Proga (2019). In particular, their sample is likely biased against sources with strong winds, which should be well represented herein.

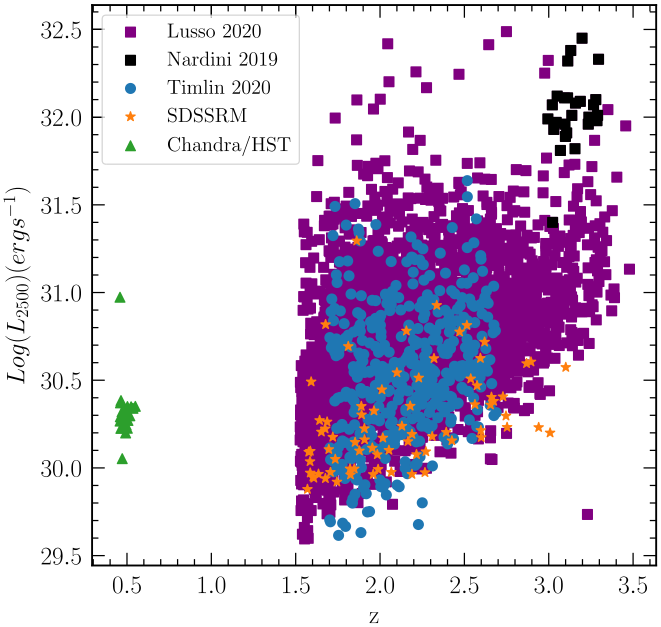

Figure 1. $\log L_{2500\,\text{Å}}$ vs. redshift for each of the X-ray subsamples included in our analysis. Our 25 Chandra/HST targets are shown as green triangles, the Timlin et al. (2020a) subset is shown with blue circles, the SDSS-RM objects are represented by orange stars, the Lusso et al. (2020) objects are represented by purple squares, and the Nardini et al. (2019) objects are represented by black squares. The bulk of the sample is contained within $1.5 < z < 3.5$ because of the need to include enough of the C IV absorption trough in the SDSS spectra to identify BAL quasars (lower limit) and to have high enough S/N spectra to perform an ICA reconstruction (upper limit).

X-ray detections, and spectral reconstructions derived from an independent component analysis (ICA). We show the range of redshift and $\log L_{2500\text{Å}}$ for each of the subsamples in Figure 1. We define a "good" subset in Section 3.4.3 with 779 objects. The origin of each of the quasar samples is specified in Table 1.

2.1. Large X-Ray Survey Data

The Timlin et al. (2020a) sample contains 2106 radio-quiet quasars at redshifts 1.7–2.7 with observations in both the Chandra archive and SDSS. They derived a "sensitive sample" of objects using the following cut on effective exposure time (in ks) and off-axis angle (arcmin), θ: $T_{\text{Eff}} >= 4.0 + 10^{\theta^2/44.89}$ (Equation (2) in Timlin et al. 2020a). They exclude BAL quasars based on the flags in Shen et al. (2011) (for quasars from SDSS DR7) and the SDSS DR12 and DR14 quasar catalogs (Pâris et al. 2012, 2014), retaining 753 objects. We use the Γ, α_{ox}, and $\Delta\alpha_{\text{ox}}$ values calculated by Timlin et al. (2020a) for the objects within this subsample.[9] The α_{ox}–L_{UV} relation from Timlin et al. (2020a) is used to calculate $\Delta\alpha_{\text{ox}}$ for the quasars in all of our subsamples (see Equation (2)); this parameter accounts for the L_{UV} dependence of X-ray emission and indicates the relative X-ray strength or weakness of a quasar of a given UV luminosity. We show both the whole sample and the sensitive sample in the interactive plots provided in Appendix C to illustrate the importance of utilizing their cut.

The Lusso et al. (2020) sample includes quasars from a 3″ cross-match between the SDSS DR14 and 4XMMDR9 catalogs (Webb et al. 2020). RL and BAL quasars were removed using the same methods as in Timlin et al. (2020a), with 349 additional quasars removed using cross-matching with the MIXR (Mingo et al. 2016) catalog, a mid-IR, radio, and X-ray catalog used to identify RL sources. After accounting for repetitions in data among their other subsets, Lusso et al. (2020) compile 13,800 unique quasars within their SDSS-4XMM sample. They identify a series of cuts used to "clean" these data, resulting in a subsample of 1644 clean quasars (their Table 1). The clean sample had the following cuts imposed on the data: (1) A minimum S/N of 1 for both the soft- and hard-band fluxes. (2) A soft-band flux limit of $F_S > 10^{15}$ erg cm s^{-1} to reduce Eddington bias. (3) Quasars with $\Gamma < 1.7$ and $\Gamma > 2.8$ were excluded, due to absorption and observational issues or contamination from the soft X-ray excess, respectively. They found that a value of $\Gamma > 2.8$ was possible if there was improper background subtraction performed for one of the two bands utilized for the calculation. (4) Finally, a cut on reddened quasars with $E(B - V) \simeq 1$ was executed (see Lusso et al. 2020 for more details on their methods). As with the Timlin et al. (2020a) sample, we show both the whole Lusso et al. (2020) sample and the clean subsamples in the plots in Appendix C; however, in our final analysis we include only the clean objects. We use the Γ values from Lusso et al. (2020) and generate α_{ox} and $\Delta\alpha_{\text{ox}}$ from their values of L_{UV} and L_X.

Table 1
Sample Statistics

Sample Name	Number of Quasars	ICA	"Good"
Lusso 2020 (SDSS-4XMM)[a]	1644	510	452
SDSS-RM (Liu 2020)	603	90	13
Timlin 2020[b]	753	443	300
Nardini 2019[c]	30	26	19
Chandra/HST	25	25	14
Total	2542	1069	779

Notes.
[a] Note that in the main paper we include only the "clean" objects from the Lusso et al. (2020) SDSS-4XMM sample; however, in the interactive plots in Appendix C we include all quasars from the SDSS-4XMM sample with ICA measurements (3461 quasars).
[b] Similarly, in the main paper we include only the "sensitive" quasars from Timlin et al. (2020a) and include all quasars from that paper with ICA measurements in the interactive plots in Appendix C (1242 quasars).
[c] The Nardini et al. (2019) sample is included within the Lusso et al. (2020) sample; these objects are only counted once toward the totals.

2.2. The SDSS-RM Sample

In order to investigate the effect of variability on the calculation of α_{ox} (see Section 3.4.1), we include a subset of the 133 SDSS-RM (Shen et al. 2015) quasars analyzed in Rivera et al. (2020),[10] which have C IV properties that were calculated from spectra using the methods of Rankine et al. (2020). We herein add measurements of the He II EQWs calculated in the same manner as Rankine et al. (2020) (see Section 3.2). These quasars each possess at least 30 epochs

[9] In Timlin et al. (2020a) observations included in the Chandra Source Catalog (CSC) were deliberately excluded to identify a sample of serendipitous sources; all of the objects they included instead have X-ray properties calculated from observations in the Chandra archive.

[10] Two errors in the pipeline used to fit and calculate the C IV EQWs resulted in (1) the flux density not being perfectly preserved across the spectra when combining the global and individual ICAs and (2) the value of $\Delta\lambda$ being incorrectly set to 1, resulting in all of the EQWs in Rivera et al. (2020) being larger by a factor of ∼2. These errors did not affect any of the trends or results from that paper, but here we use the correct EQWs.

of SDSS spectra taken over the course of a few months during 3 consecutive years (2014–2016). We use the XMM-RM catalog released by Liu et al. (2020) to calculate Γ, $\alpha_{\rm ox}$, and $\Delta\alpha_{\rm ox}$ values for this sample. The methods used to calculate these values are very similar to those used for the Chandra sample, given in Appendix B; however, we modeled the flux ratios (F_H/F_S) instead of hardness ratios (HRs) to calculate Γ. The number of matches between the Rivera et al. (2020) and Liu et al. (2020) samples is 96 quasars, 75 of which had detections in both the hard and soft bands for computing Γ values.

2.3. Subsamples at Constant Luminosity and Redshift

In an effort to offset the bias against wind-dominated quasars in the low-z classical reverberation-mapped AGN sample (Figure 18, Richards et al. 2011), we selected 25 quasars for new observations with both HST and Chandra. These quasars are at $z \sim 0.5$. Their C IV measurements are derived from HST rather than SDSS, but the same Rankine et al. (2020) ICA components are used to generate the spectrum reconstructions from which measurements are made. Details of the analysis of the HST and Chandra data for these targets are included in Appendices A and B, respectively, including tables describing their UV and X-ray properties.

A subsample of the Lusso et al. (2020) data was analyzed by Nardini et al. (2019) and Lusso et al. (2021), who argued that some sources must be intrinsically X-ray weak rather than absorbed. As with our Chandra/HST sources, these objects were selected as bright blue quasars. However, these quasars are high L and high z rather than low L and low z, and a significant fraction (∼25%) are unusually X-ray weak, with the sample covering a large range in Γ and $\Delta\alpha_{\rm ox}$. These 30 quasars are between $z = 3.0$ and 3.3 and have $\log(L_{2500\,\text{Å}}) \sim 32$, and they are marked as a separate subsample from Lusso et al. (2020) in all of the figures in which subsamples are denoted.

2.4. UV Line Parameters from Spectral Reconstructions

Rankine et al. (2020) examine ≈144,000 SDSS DR14 quasars between redshifts ≈1.57 and 3.5 (the lower limit set to allow for BAL classifications based on the C IV line) and with an average spectral $S/N \geqslant 5$ (per 69 km s^{-1} pixel). The upper redshift limit of $z < 3.5$ was chosen as a result of the reduction in S/N in the SDSS spectra covering the C III] emission at higher redshifts. Matching between Rankine et al. (2020) and Timlin et al. (2020a) to retrieve the ICA-based C IV EQWs and blueshifts and to add He II EQWs from Rankine et al. (2020) further reduces this sample from 753 to 443, as these were the number of quasars that overlapped from the two samples given the Rankine et al. (2020) S/N cut. We similarly find 3461 matches between the Lusso et al. (2020) and Rankine et al. (2020) data sets, 510 of which are included in the "clean sample" of Lusso et al. (2020).

2.5. Overview of Data

Each of the subsamples we use were chosen to address specific questions. The Timlin et al. (2020a) sensitive sample is well controlled for effects arising from off-axis objects; however, the sample contains quasars that are likely more absorbed than those contained within the Lusso et al. (2020) clean sample. In addition to being careful about identifying and removing absorbed quasars, the Lusso et al. (2020) sample expands the range of z and L. The SDSS-RM sample can be used to address issues of variability in the UV; however, it is otherwise comparable to the Lusso et al. (2020) objects (though the SDSS-RM quasars are contained within a smaller area). The Chandra/HST and Nardini et al. (2019) samples allow us to investigate the effects of luminosity and redshift by focusing on (and between) two small ranges that are widely separated. We unify the data sets to enable a more in-depth investigation, creating a relatively uniform analysis of optical/UV and X-ray properties of the largest possible sample of SDSS quasars, using X-ray data from Chandra and XMM-Newton. The C IV measurements from Rankine et al. (2020) allow us to create a uniform framework for measuring C IV properties that are not affected by the presence of absorption features and with improved S/N, compared to the original spectra. We apply uniform cuts across our overall sample to identify the most robust sample that reflects intrinsic quasar physics in a way that is not obscured by absorption.

3. UV/X-Ray Features

Before comparing trends in observed properties to physical models, we must first address the sources of scatter that may obscure such trends. In Section 3.1 we define the C IV parameter space and describe its nonlinear nature. We then derive two new C IV distance parameters that each incorporate information from the C IV EQWs and blueshifts to address this nonlinearity and allow for clearer correlations with other parameters. Section 3.2 addresses our use of UV spectra reconstructed from ICA to improve the S/N and determination of redshifts for these data (thereby improving the accuracy of the measured EQWs and blueshifts). In Section 3.3, we present the X-ray parameters we use and explore their trends with optical luminosity. Finally, in Section 3.4 we discuss how optical/UV/X-ray parameters can be corrupted and the importance of applying corrections or censoring the data before carrying out further correlation analysis.

3.1. The C IV Parameter Space

The C IV parameter space (C IV EQW vs. C IV blueshift, shown in Figure 2) is used to sort quasars at high redshift from disk-dominated to wind-dominated quasars (e.g., Richards et al. 2011), which may be equivalent to sorting from low to high $L/L_{\rm Edd}$ as the C IV parameters change. Indeed, each of the C IV parameters on their own has been shown to correlate with the physical properties of quasars, such as L and $L/L_{\rm Edd}$. Specifically, the C IV EQW is anticorrelated with the luminosity of a quasar (Baldwin 1977; Dietrich et al. 2002), albeit with a large amount of scatter. Moreover, there is evidence suggesting that the C IV EQW is more strongly anticorrelated with $L/L_{\rm Edd}$ (the "modified Baldwin effect" or MBE; Shemmer & Lieber 2015). However, Shemmer & Lieber (2015) find that this relationship breaks down for the lowest-EQW sources, which may be consistent with the finding of Rankine et al. (2020, Figure 14) that $L/L_{\rm Edd}$ correlates with the C IV blueshift at high blueshifts (and thus low EQW).

While the C IV parameter space is useful in separating quasars at the extremes of $L/L_{\rm Edd}$, intermediate populations are harder to distinguish from one another. In order to (1) address the nonlinearity inherently present in the C IV parameter space and (2) help identify which parameters drive changes in the C IV parameter space, we derive two measurements of C IV distance, one parallel and one perpendicular to a best-fit curve in the C IV parameter space. Motivation for such a decomposition of the C IV parameter space comes from Figure 12 of

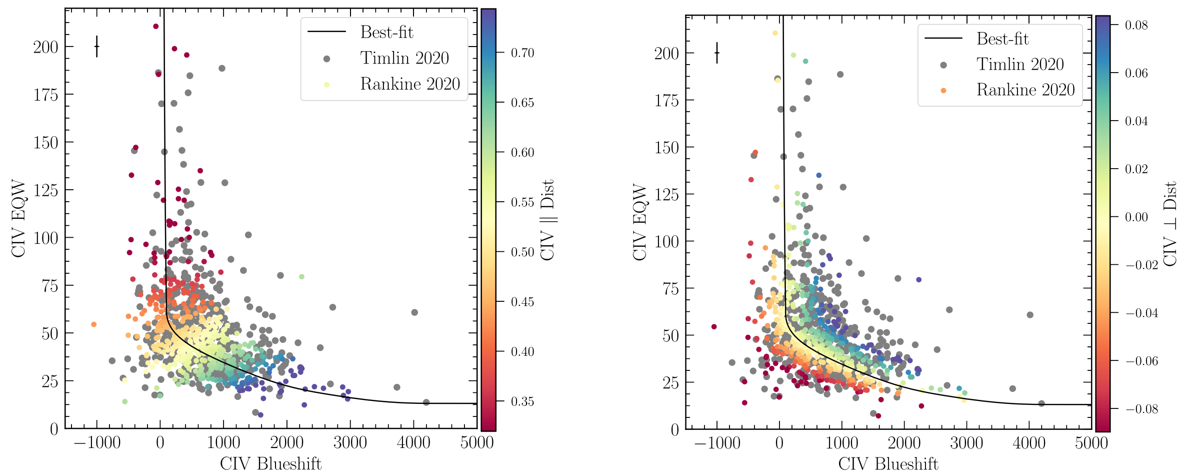

Figure 2. Left: the C IV parameter space of our subset of Timlin et al. (2020a) quasars with the C IV EQWs and blueshifts from that same paper shown as the gray circles, and the ICA-generated C IV parameters colored by the C IV ∥ distance. The best-fit line to the ICA-generated C IV EQW and C IV blueshift space is shown as the solid black curve. Right: same as the left panel, but colored by the C IV ⊥ distance.

Rankine et al. (2020), which shows a smooth gradient of He II EQW across the C IV parameter space with constant He II EQW tangent to that gradient. While He II EQW is a known high-quality indicator of the hardness of the quasar SED, in contrast to C IV, it is a relatively weak line, and therefore it is harder to measure its EQW accurately. We thus define the C IV ∥ and C IV ⊥ distances to respectively parameterize (without reference to the He II emission line) the physics behind the gradient and behind quasars with equivalent He II but very different C IV properties.

The best-fit curve to the C IV parameter space is constructed by piecewise polynomial fitting to the Rankine et al. (2020) sample and shown as the black line in Figure 2; for details see McCaffrey & Richards (2021). The fit is forced to be linear above an EQW of 60 Å owing to the small number of sources and the unconstrained fit being linear but noisy. To generate the C IV parallel and perpendicular distances, we first use the `MinMaxScaler` built into `scikit-learn` (Pedregosa et al. 2011) to transform the data values for each axis (EQW and blueshift) from 0 to 1; this scaling ensures that equal weight is given to both parameters in computing C IV distances. The C IV ∥ distances were measured relative to the first point on the best-fit curve (i.e., in the upper left corner at C IV EQW $\simeq$316 Å and C IV blueshift $\simeq$50 km s^{-1}). The C IV ⊥ distance was measured relative to the closest (projected) point on the curve. The C IV parameter space colored by these hybrid metrics is shown in Figure 2. For discussion on the utility of using the C IV ∥ distance as an SED indicator, see Section 4.3.

3.2. ICA Reconstructions

Spectral principal component analysis (PCA) is a common data analysis technique in which a linear combination of spectral components can be used to reconstruct spectra (Francis et al. 1992; Yip et al. 2004). ICA is lesser known but similarly capable of reconstructing spectra; however, unlike PCA, ICA components are not required to be orthogonal to each other and are thus potentially more physically meaningful. Rankine et al. (2020) used their large sample of SDSS DR14 quasars to derive ICA components capable of reconstructing both BAL and non-BAL quasar spectra and generated line parameters from these spectra.

All of the data that we use (including for quasars from the literature) have reconstructions derived using an ICA of SDSS DR14 spectra available from Rankine et al. (2020), from which we take our final C IV EQW and blueshift values. The redshifts for the quasars were derived using an ICA reconstruction of the C III] emission complex and Mg II emission (when available) with the quasar redshift left as a free parameter. For quasars with redshifts $z < 1.1$ the results are essentially identical to those of Hewett & Wild (2010). For larger redshifts the results represent a significant improvement over the Hewett & Wild (2010) values, and the deliberate exclusion of the C IV emission line here is key. There are several advantages to the use of the ICA reconstructions for our analysis: (1) the method uses information from other emission lines (such as the C III] complex), essentially as priors, to reconstruct the C IV line; and (2) the reconstructions effectively increase the S/N of the spectra in the region of interest.

To calculate the EQWs and blueshifts for the C IV line, we use the same procedure as Coatman et al. (2016), with the exception that here we take nonparametric measurements directly from the reconstructed spectra. A power-law continuum fit was constructed locally from 1445–1465 Å and 1700–1705 Å. The integration window for measuring the EQW was 1500–1600 Å, except for high-blueshift objects, for which the window was extended down to 1465 Å. To calculate the blueshifts, we use the equation C IV blueshift (km s^{-1}) = $c(1549.48 - \lambda_{\rm half})/1549.48$, where 1549.48 Å is the rest-frame wavelength for C IV and $\lambda_{\rm half}$ is the wavelength that bisects the integrated flux. A power-law continuum fit was similarly constructed locally for the He II line in the ranges 1610–1620 Å and 1700–1705 Å, with the limits of integration for EQW calculation set to 1620 and 1650 Å. Investigating trends within C IV/X-ray parameter space with both the Timlin et al. (2020a) and Rankine et al. (2020) C IV EQWs and blueshifts yields a difference in the rms values of the C IV ∥ distances of 0.48 (improvement shown in Figure 2). We use the Rankine et al. (2020) line parameters for all of the data samples in the remainder of this paper. We assume here the same errors as were calculated in Rivera et al. (2020), derived from executing a Monte Carlo approach. The continuum fit for every epoch for every SDSS-RM quasar was altered by a random contribution from the flux error array 50 times, and the 1σ error for the resulting EQWs and blueshifts was generated as the standard deviation of those values. The error bars themselves are equal to 2 times the median of these standard deviations. These error bars are shown in Figure 2. It is important to note that this is the minimum error considering that it was derived from multiepoch data, whereas most of the data

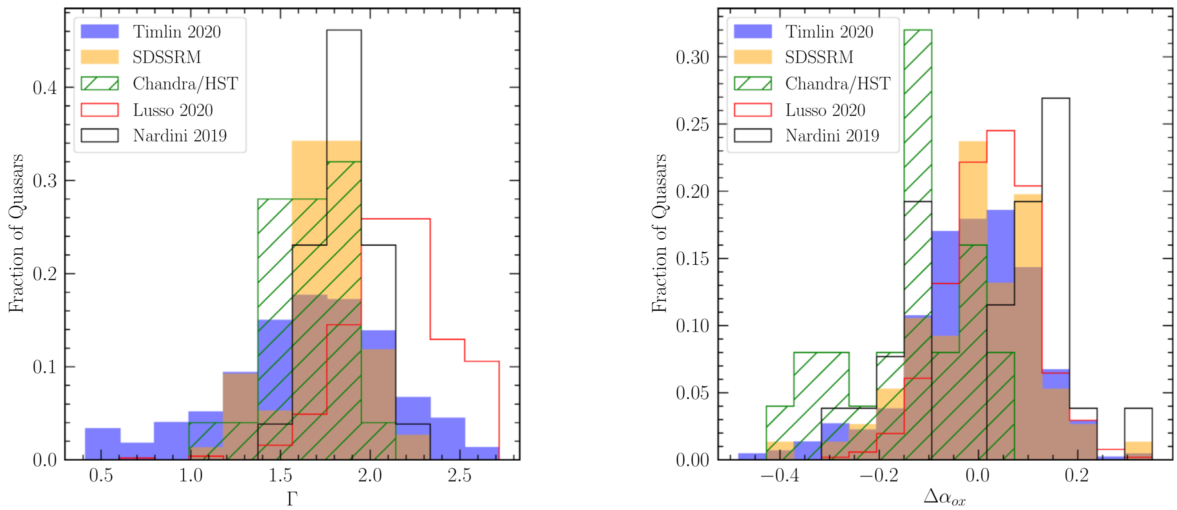

Figure 3. Left: histogram of Γ values for our main sample. It is important to keep in mind that the Γ values included herein are estimates calculated from HRs and have larger errors than Γ values measured directly from the X-ray spectra. Right: histogram of $\Delta\alpha_{\rm ox}$ values for our sample. The distribution is similar to that shown in Figure 4 of Gibson et al. (2008), which consists of RQ, non-BAL quasars.

contained within are single epoch in nature. Additionally, this error bar only includes the uncertainty resulting from the continuum fit and does not include the error in the derived redshift.

3.3. X-Ray Features

While we probe the wind with UV spectra features, the X-ray allows us to study the corona (pink in Figure 1 of Giustini & Proga 2019) through the X-ray spectral index, Γ, and the connection between the corona and accretion disk (green in Figure 1 of Giustini & Proga 2019) through the optical-to-X-ray spectral slope, $\alpha_{\rm ox}$. A histogram of the Γ values of our sample is shown in the left panel of Figure 3. Caution is needed: the most reliable method of measuring Γ is directly from the spectra when the number of observed counts is high (for Chandra and XMM-Newton, >100 counts). Spectral fitting is possible in the case of lower counts; however, the uncertainties become larger. As the majority of the objects in our sample possess fewer counts, it is outside of the scope of this work to perform spectral fitting on the large sample contained herein. We instead approximate Γ using hardness/flux ratios, as shown in Appendix B to be consistent with the studies of Timlin et al. (2020a) and Lusso et al. (2020). Unfortunately, the errors on such approximations can be very large, ±0.5 or more.

The $\alpha_{\rm ox}$ parameter is defined as $\alpha_{\rm ox} = 0.384\log(\frac{L_{\rm 2keV}}{L_{2500\,\text{Å}}})$ (Tananbaum et al. 1979). However, because $\alpha_{\rm ox}$ is anticorrelated with L (Steffen et al. 2006), a histogram of values is not as meaningful as it would be for Γ. To remove this luminosity dependence, it is standard to calculate $\Delta\alpha_{\rm ox}$ (Gallagher et al. 2006), the difference between the measured and expected $\alpha_{\rm ox}$ values. Empirically, the expected $\alpha_{\rm ox}$ as a function of monochromatic 2500 Å luminosity, $L_{2500\,\text{Å}}$, is given by Equation (3) from Timlin et al. (2020a) as

$$\alpha_{\rm ox} = (-0.199 \pm 0.011)\,{\rm Log}(L_{2500\,\text{Å}}) + (4.573 \pm 0.333)\,\sigma_\epsilon = 0.11. \quad (2)$$

σ_ϵ is the intrinsic dispersion in the relationship. The $\Delta\alpha_{\rm ox}$ distribution of our sample is shown in the right panel of Figure 3. The $\Delta\alpha_{\rm ox}$ distribution is consistent with the sample of radio-quiet (RQ), non-BAL quasars shown in Figure 4 of Gibson et al. (2008). Sources with $\Delta\alpha_{\rm ox}$ lower than −0.2 are generally considered X-ray weak (whether intrinsically X-ray weak or absorbed). In Section 3.4.3, we discuss how we use Γ and $\Delta\alpha_{\rm ox}$ to identify quasars experiencing absorption.

3.4. Corrections to UV/X-Ray Features

3.4.1. Variability

To test the effect of UV variability on the calculation of $\alpha_{\rm ox}$, we look at the behavior of the changing values of $L_{2500\,\text{Å}}$ and the resulting impact on the calculation of $\alpha_{\rm ox}$ and $\Delta\alpha_{\rm ox}$ of the 75 SDSS-RM quasars from Rivera et al. (2020) over time. We calculated the flux density at 2500 Å directly from the SDSS DR14 spectra. The flux calibration of the DR14 spectra has a relatively high uncertainty in the spectral flux calibration as a function of wavelength (Margala et al. 2016). As a consequence, quasar spectra were processed using the scheme described in Rivera et al. (2020, Section 2.3 and Figure 2). The bottom panel of Figure 4 shows the tracks of those objects within the $\alpha_{\rm ox}$–$L_{2500\,\text{Å}}$ parameter space over time, colored by their C IV ∥ distance values. Keeping in mind that we do not have simultaneous observations of changes in the X-ray, the UV variability affects the slope of a single object in $\alpha_{\rm ox}$–$L_{\rm UV}$ space such that the observed $\alpha_{\rm ox}$ values will change more rapidly than expected based on the global fit to the sample. The average change in $L_{2500\,\text{Å}}$ is about 0.1 dex, and the average change in $\alpha_{\rm ox}$ was 0.08.

Since we do not have individual X-ray measurements for the various epochs, we additionally approximate the effect of X-ray variability on the sample using the same method as detailed in Timlin et al. (2021b). First, we add in quadrature 36% uncertainty of $L_{\rm 2keV}$ to the measurement uncertainty on $L_{\rm 2keV}$. The additional 36% uncertainty is the median absolute deviation of the long-timescale X-ray variability distribution included in Timlin et al. (2020b). Assuming that the X-ray and UV are uncorrelated leads to a change in $\alpha_{\rm ox}$ of ∼0.08 from just the X-ray variability alone. Using the error propagation methods of Lyons (1991, see Section 1.7.3), we find that the typical error in $\alpha_{\rm ox}$ can be as high as 0.19 and the error in $\Delta\alpha_{\rm ox}$ as high as 0.08.

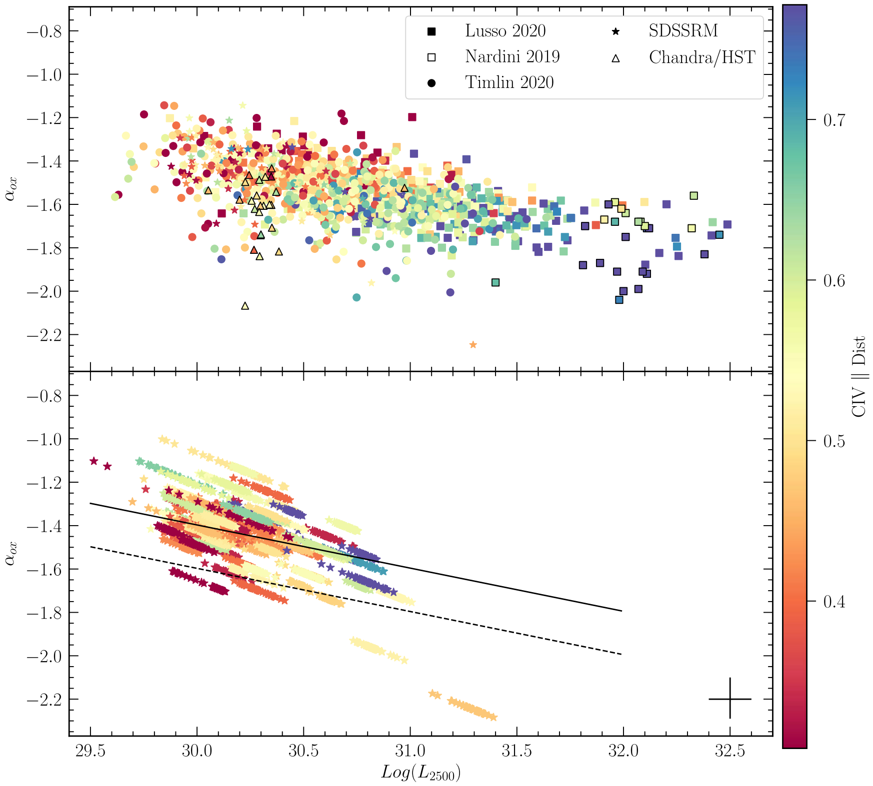

Figure 4. Top: all of our sample objects plotted in $\alpha_{\rm ox}$–$L_{2500\ \mathring{A}}$ space. The objects from Timlin et al. (2020a) are shown as circles, our Chandra/HST objects as triangles, the median values for the SDSS-RM targets from Rivera et al. (2020) as stars, and the Lusso et al. (2020) objects as squares. The Chandra/HST and Nardini et al. (2019) objects are highlighted in black to illustrate the samples with a small range of luminosity. Bottom: all values of $\alpha_{\rm ox}$ and $L_{2500\ \mathring{A}}$ calculated for the SDSS-RM objects. The colored tracks indicate the variability in $L_{2500\ \mathring{A}}$. The best fit from Timlin et al. (2020a) is shown as the solid black line; the dotted line shows the boundary for X-ray-weak quasars with $\Delta\alpha_{\rm ox}$ values $<=-0.2$. The points in both panels are colored by the C IV || distance. The plus sign in the lower right corner in the bottom panel shows the median errors for the SDSS-RM sample.

3.4.2. Reddening

In the same way that the X-ray can be affected by absorption, the UV may be affected by dust reddening. However, because the dust-to-gas ratio in X-ray absorbers is likely to be low and is difficult to measure, and because the UV and X-ray lines of sight are not necessarily the same through the absorber, we do not alter $L_{\rm UV}$ based on the inferred column density of gas in the X-ray. Instead, we identify potentially dusty objects (which will appear to have lower L_{2500} than is intrinsic) in two ways. One is using the Γ_1, Γ_2 prescription (based on the slopes from rest frame 0.3–1 μm and 1450–3000 Å, respectively) of Lusso et al. (2020), which is only relevant herein for the definition of the "Lusso Clean" subsample. The other is using $\Delta(g-i)$ following Richards et al. (2003), where the redshift-corrected colors are determined from the SDSS g- and i-band point-spread function photometry (see also Krawczyk et al. 2015; also shown in Figure 5). An asymmetric tail to higher values as compared to $\Delta(g-i)<0$ would be indicative of dust reddening. This asymmetry is not strong in our data, perhaps due to the cuts that were already applied to the Lusso et al. (2020) and Timlin et al. (2020a) samples.

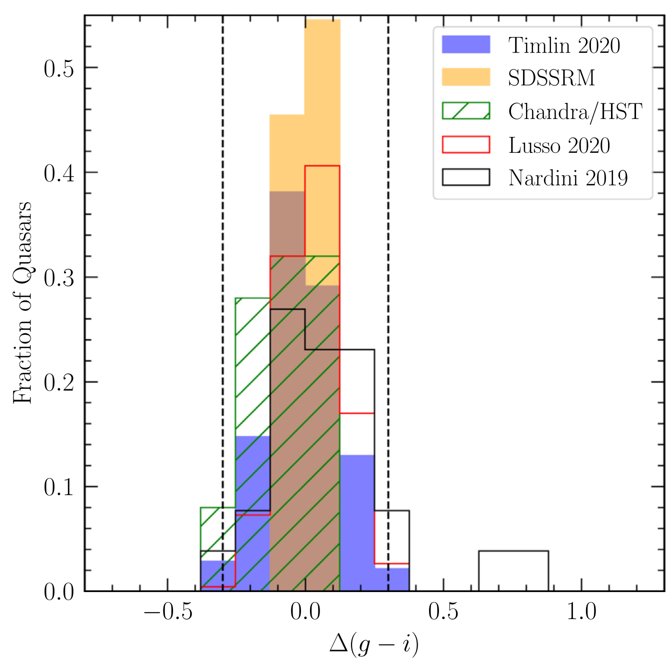

Figure 5. Histogram of $\Delta(g-i)$ values for our sample. Objects that are more likely to be dust reddened (as opposed to intrinsically red) will have larger values in the red (right) tail of the $\Delta(g-i)$ distribution.

3.4.3. X-Ray Weakness and the Effect of Absorption

With the cleanest possible measurements of C IV in hand (derived from survey-depth, single-epoch spectra), we explore the connection between X-ray properties and UV emission properties. Figures 4 and 8 of Kruczek et al. (2011) show the average values of $\Delta\alpha_{\rm ox}$ (Γ) decreasing (increasing) from the upper left corner of the C IV parameter space to the lower right corner, which we replicate in Figure 6. While there is a general trend in these parameters across the C IV space, a wide range of

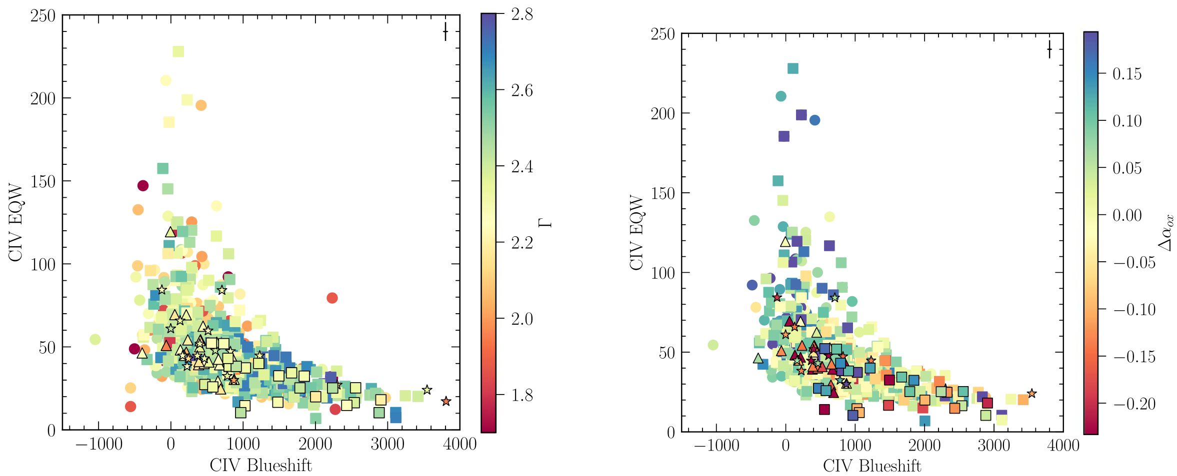

Figure 6. Left: C IV parameter space colored by Γ. Right: C IV parameter space colored by $\Delta\alpha_{\rm ox}$. The error bars are the same as those used for Figure 2. The markers are the same as for the top panel of Figure 4. The Chandra/HST sample, the SDSS-RM sample, and the Nardini et al. (2019) sample are highlighted in black. Though general trends exist in both parameter spaces, outliers are possible at all values of C IV EQW and blueshift.

$\Delta\alpha_{\rm ox}$ and Γ values are possible at all values of EQW and blueshift. Because of the role played by absorption from gas and reddening from dust, caution is needed in interpreting these plots. Examining Γ and $\Delta\alpha_{\rm ox}$ together has more diagnostic power to identify the presence of absorption (particularly at high z or relatively low column densities) than either parameter alone. If an object possesses a low Γ value and has a $\Delta\alpha_{\rm ox}$ value indicative of being X-ray weak, then the object is likely to be absorbed. However, if an object's Γ value is relatively normal and it has a low $\Delta\alpha_{\rm ox}$, then the object is likely intrinsically X-ray weak. The Γ–$\Delta\alpha_{\rm ox}$ distribution is shown in Figure 7. The Γ errors shown are the standard deviation for each source of data. The Timlin and Chandra/HST objects share the same error bar, as the same method was used to generate Γ values for these samples. We demonstrate the possible effects of different amounts of absorption for a neutral absorber with an absorbed power-law model with the gray solid lines. Each absorption track is for a different redshift, with the redshift increasing from left to right in steps of 0.5 from 0.5 to 2.5. Absorption is stronger the farther one travels downward and left along a track, with values of $N_H = 0.1$, 0.2, 0.5, 1, 2, and 5×10^{23} cm^{-2} being marked respectively by the black sideways triangles. A Γ value of 2 was used to derive these curves. If a value of $\Gamma = 2.2$ were instead used, the curve would be slightly above and to the left of the $\Gamma = 2$ curve, much in the same way the curve shifts from $z = 2.5$ to $z = 2$. If a value of $\Gamma = 1.8$ were used, the curve would instead be slightly lower and to the right.

Two interesting trends are revealed by Figure 7. First, there is a gradient in C IV distance largely perpendicular to the absorption tracks. As will be discussed further in Section 4.4, that observation is interesting in that both Γ and C IV distance are possible indicators of $L/L_{\rm Edd}$, yet they are nearly orthogonal. The second is that the data roughly follow the absorption tracks with decreasing Γ. This trend suggests a more robust way to limit absorbed objects (while including objects with smaller intrinsic Γ), by cutting not on Γ itself (as in Lusso et al. 2020) but instead in this 2-D parameter space. We cut the data below a diagonal line at

$$\Gamma = -1.38 * \Delta\alpha_{\rm ox} + 1.376, \tag{3}$$

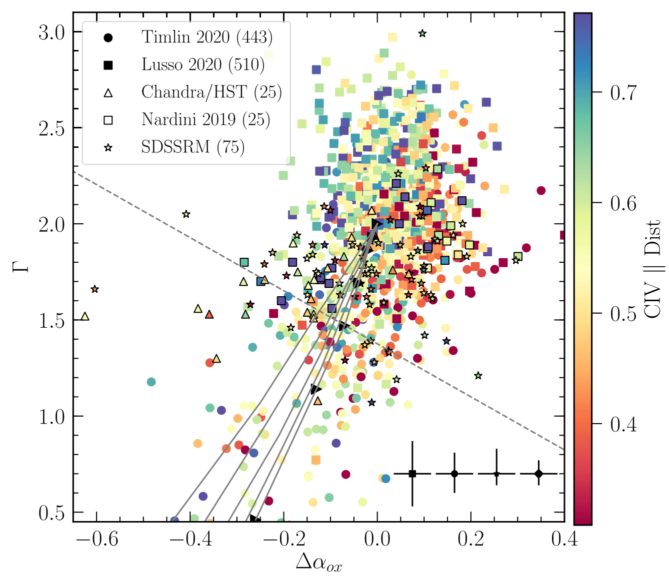

Figure 7. Γ vs. $\Delta\alpha_{\rm ox}$ values for all of the objects in our sample. The markers have the same designation as the top panel in Figure 4. The Chandra/HST, SDSS-RM, and Nardini et al. (2019) samples are highlighted in black to distinguish them from the rest of the distribution. The cut we implement as a function of both Γ and $\Delta\alpha_{\rm ox}$ is shown as the diagonal gray dashed line. Tracks showing the effects of varying levels of absorption are shown by the solid gray lines. The absorption increases down and to the left along each track, as shown by the black sideways triangles on the $z = 2.5$ track, with values of $N_H = 0.1$, 0.2, 0.5, 1, 2, and 5×10^{23} cm^{-2}, respectively. The redshift increases from the left track to the right from 0.5 to 2.5 in steps of 0.5. These tracks shown are indicative of a neutral absorber; however, for absorbers that are complex or partially ionized we would expect less of a reduction on Γ as the absorber column density increases, as these absorbers are not capable of blocking all incoming soft photons (Gallagher et al. 2006). The data points are colored by the C IV ∥ distance and illustrate a connection between the X-ray and emission-line properties of quasars.

shown by the gray dotted line in Figure 7. As a check for biases, we examined several spectra with sufficient counts for spectral analysis beneath this absorption cut, and all were absorbed. While there are large uncertainties in our Γ values, our HR Γ values are being used primarily with $\Delta\alpha_{\rm ox}$ to identify absorbed quasars and help clean the $\alpha_{\rm ox} - L_{\rm UV}$ correlation. They appear to be adequate for that purpose, based on the absorption tracks and trends in C IV ∥ distance shown in

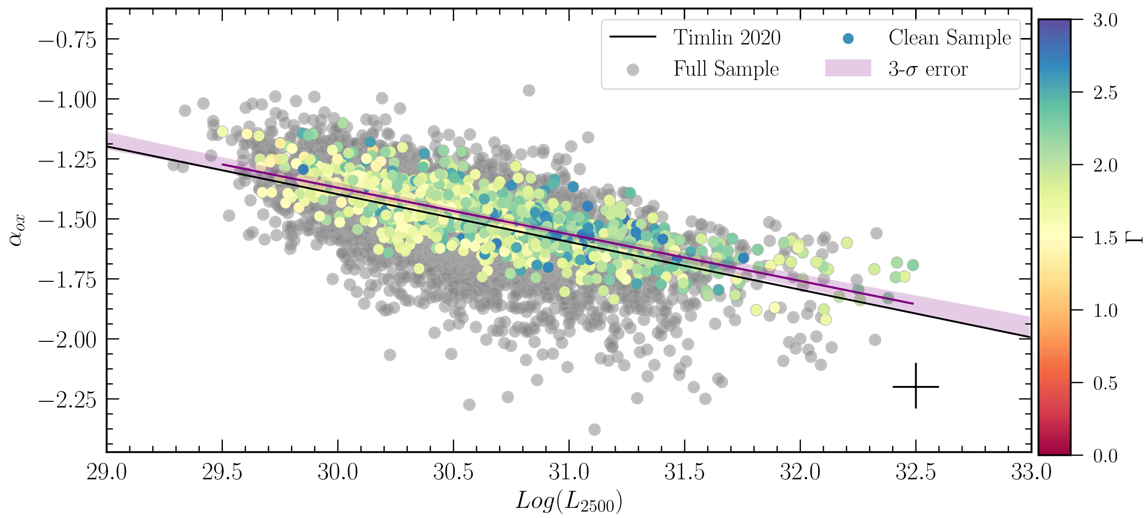

Figure 8. The overall sample in α_{ox}–L_{UV} space (gray points), and our "clean" subsample of quasars (colored points) used to generate a new fit (purple line) to the α_{ox}–$L_{2500\ \text{Å}}$ relation. The points are colored by their Γ values. The relation derived in Timlin et al. (2020a) is shown as the black solid line for reference.

Figure 7. In addition to this cut and the reddening cut above, we endeavor to ensure that our trends are not contaminated by absorbed objects (in either the UV or X-ray) by further removing the quasars with $\Delta\alpha_{ox}$ values <-0.3. We additionally remove quasars with $\Delta\alpha_{ox}>0.3$. Finally, we cut on quasars that could potentially be contaminated by the soft X-ray excess (keeping quasars with $\Gamma<2.8$, excluding quasars in the Lusso et al. 2020 sample that they removed in their "clean cuts" as mentioned in Section 2.1; only two quasars in our other samples do not meet this criterion). The union of these cuts and the requirement that each quasar possesses ICA-generated He II EQW and C IV EQW and blueshift values are used to define a "Good" subsample (see Appendix C).

With these cuts in place, we generate the α_{ox}–$L_{2500\ \text{Å}}$ relation for our sample. We use the `linmix` interpretation of the Bayesian fitting method developed by Kelly (2007) to perform the fit. `linmix` fits a linear model to a univariate distribution and outputs the model, its associated confidence interval, and an estimate of the intrinsic scatter. The best-fit relation for our sample is

$$\alpha_{ox} = (-0.194 \pm 0.0057)\log(L_{2500\text{Å}}) + (4.451 \pm 0.1737),\ \sigma_{\epsilon} = 0.09. \quad (4)$$

The full sample (gray points), the subsample we use for the fit (colored points), the range of their Γ values, and the relation (purple solid line) are shown in Figure 8. While there is a reduction in the intrinsic dispersion in the relationship, our new fit is otherwise not very different from the Timlin et al. (2020a) relation (shown in black for a comparison). This similarity may be due to the fact that Timlin et al. (2020a) fit to their "sensitive sample" of quasars, in which they have already removed data of lower quality. We chose to continue to use the $\Delta\alpha_{ox}$ values calculated from the Timlin et al. (2020a) relation. However, we note here that if the relation is calculated with a simple Γ cut instead of a cut on $\Delta\alpha_{ox}$, the dispersion instead becomes 0.11, and if no cuts are enacted at all, it becomes 0.13.

A quasar's redshift affects the energies that are probed in the X-ray. At higher redshift, softer X-rays drop out of the observed band. This shift in observed energies reduces the contribution from the soft X-ray excess (see Section 1) and also reduces the effect of absorption on Γ and $\Delta\alpha_{ox}$ (see the increase in the steepness of the slopes of the gray tracks with increasing redshift in Figure 7). While the reduction in the effects of absorption should make it easier to distinguish between quasars at high and low accretion rate (from the correlation of Γ and L/L_{Edd}), the reduction in contribution from the soft X-ray excess makes it more difficult to separate out objects at low mass and low accretion rate and objects at high mass and high accretion rate, as these two groups of objects are expected to have strong and weak contributions from the soft X-ray excess (see Figure 2 of Giustini & Proga 2019).

4. Discussion

4.1. Implications for Cosmology

Risaliti & Lusso (2015) have developed a method for using quasars to constrain cosmological parameters. Their method depends on the nonlinear relationship between X-ray and optical/UV luminosity and reducing possible sources of scatter in α_{ox}. Scatter could come in the form of dust reddening or gas absorption and/or variability between the optical and X-ray epochs. Lusso et al. (2020) remove absorbed objects by making a cut in Γ, while Figure 7 illustrates that cutting in the Γ versus $\Delta\alpha_{ox}$ plane, as is done herein, is more appropriate.

Figure 7 illustrates that there is potential for applying a correction in addition to (or instead of) cutting absorbed objects —even after accounting for the trend in luminosity, as $\Delta\alpha_{ox}$ is a function of both Γ and the C IV ∥ distance. From Figure 7 it would appear that a simple multidimensional linear fit to $\Delta\alpha_{ox}$ as a function of both Γ and the C IV ∥ distance could be used to make corrections to α_{ox} for individual objects in a way that would further reduce the scatter in the (corrected) α_{ox} distribution. We will attempt this approach in future work, as it is beyond the scope of this paper. Doing so could enable the development of a relationship similar to that of Phillips (1993) (which allows for Type Ia supernovae to have a "standardizable" luminosity) to further reduce the scatter in α_{ox} for the sake of the Risaliti & Lusso (2015) method.

Moreover, we note that if there is a universal trend between C IV ∥ distance and α_{ox} that is obscured by variability, it is more likely that the measurement of α_{ox} would be affected than

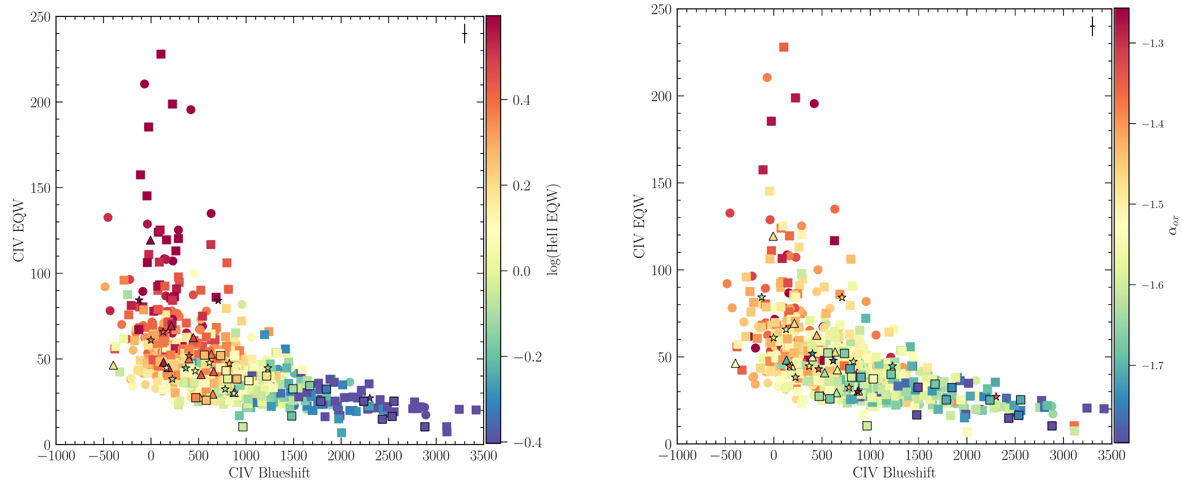

Figure 9. Left: C IV parameter space for our sample colored by the log of He II EQW. The error bars are the same as in Figure 2. Right: same plot colored by $\alpha_{\rm ox}$ instead. The markers are the same as the top panel of Figure 4. Despite our cut on Γ to remove absorbed objects, it is clear that there are still factors that affect the usefulness of $\alpha_{\rm ox}$ as an indicator of the shape of the ionizing SED in comparison to the log of He II EQW, such as variability.

the measurement of C IV ∥ distance. Thus, quasars that are on the "wrong" side of the diagonal in Figure 7 (having large C IV ∥ distance on the right or small C IV ∥ distance on the left) may be indicative of sources where $\alpha_{\rm ox}$ is affected by variability and could be removed from the cosmological analyses.

4.2. Quasars at Constant Luminosity and Redshift

With our Chandra/HST sample we sought to identify a sample at low z and low L that was intended to be as unbiased as possible to winds. The resulting empirical lack of large blueshifts among these objects suggests a lack of strong winds, which may be due to a luminosity dependence on wind driving (Veilleux et al. 2013; Zakamska & Greene 2014). Despite the selection criteria limiting our sample to bright, blue sources (necessary given the "expense" of HST time), nearly all of these objects have negative values of $\Delta\alpha_{\rm ox}$, and eight of them are formally X-ray weak with $\Delta\alpha_{\rm ox} < -0.2$. The Nardini et al. (2019) sample, also selected as bright, blue quasars but at much higher luminosity, similarly possesses a large fraction of X-ray-weak ($\Delta\alpha_{\rm ox} < -0.2$) objects (≈25%).

The locations of our 25 Chandra/HST targets and the Nardini et al. (2019) sample in C IV parameter space colored by Γ and $\Delta\alpha_{\rm ox}$ relative to the whole sample are shown in the left and right panels of Figure 6, respectively. Combining these data with the larger sample, we look to examine their UV and X-ray properties in the context of theoretical models describing the dominant physical mechanisms of quasars in different accretion rate and mass bins.

Nardini et al. (2019) suggest that their X-ray weak quasars possess strong accretion disk winds with coronae in a radiatively inefficient phase—due to the fact that their spectra were better fit without contributions from absorption. In this scenario, a significant amount of the gravitational energy from infalling material that would normally be converted to UV and optical radiation in the form of seed photons for Compton upscattering is used to supply the wind with the necessary thrust to launch. We explore these sources further in Appendix C, while the work of Marlar et al. (2022) considers the Chandra/HST sample in context with a different sample of objects.

4.3. SED Indicators

$\alpha_{\rm ox}$ and the He II EQW are known to be indicators of a quasar's SED, with the He II EQW indicating the strength of the SED at 54.4 eV and $\alpha_{\rm ox}$ describing the global slope of the 2500 Å (5 eV) through 2 keV range of the SED. These two parameters probe different SED physics, as the harder X-ray photons, which are used in the calculation of $\alpha_{\rm ox}$, are thought to be created in an X-ray corona above the accretion disk. In contrast, the ionizing extreme-ultraviolet (EUV) photons are thought to be generated within the inner accretion disk. Indeed, the X-ray emission utilized in the computation of $\alpha_{\rm ox}$ should not strongly affect He II production. However, Timlin et al. (2021b) found that there remains a relationship between the He II EQW and $\alpha_{\rm ox}$ after accounting for luminosity, indicating that the strength of the production mechanism for both of these regions is tied together. Hence, we investigate the pros and cons of using He II and $\alpha_{\rm ox}$ as indicators of the ionizing SED—as well as a parameter that behaves in a similar manner: the C IV ∥ distance. One might expect the He II EQW and C IV ∥ distance to correlate, as it was noted by Baskin et al. (2013) and Baskin et al. (2015) that a decrease in He II EQW was correlated with an increase in the C IV blueshift for both BAL and non-BAL quasars. The left panel of Figure 9 illustrates the systematic gradient of He II EQW in C IV space previously demonstrated by Rankine et al. (2020), which resulted from the careful analysis of ≃144,000 quasars using ICA reconstructions.[11]

Both C IV and He II are dependent on how strong the ionizing EUV emission is; however, the excitation mechanisms for each are different. The C IV line is a secondary indicator of the shape of the SED, as the C IV ions are produced by electron −ion collisions that are sensitive to the temperature of the gas. In contrast, the strength of the He II line is determined by the He II to He III ionization rate, as He II is formed by the recombination of He III to He II (Timlin et al. 2021b) and is a more direct indicator of the ionizing continuum. An additional impediment to using the C IV EQW as an SED indicator is that

[11] Note that the large number of quasars in the Rankine et al. (2020) sample allowed for each hexbin in their Figure 12 to consist of an average over the He II EQWs of multiple quasars, resulting in a smoother trend of the C IV parameter space with log(He II EQW).

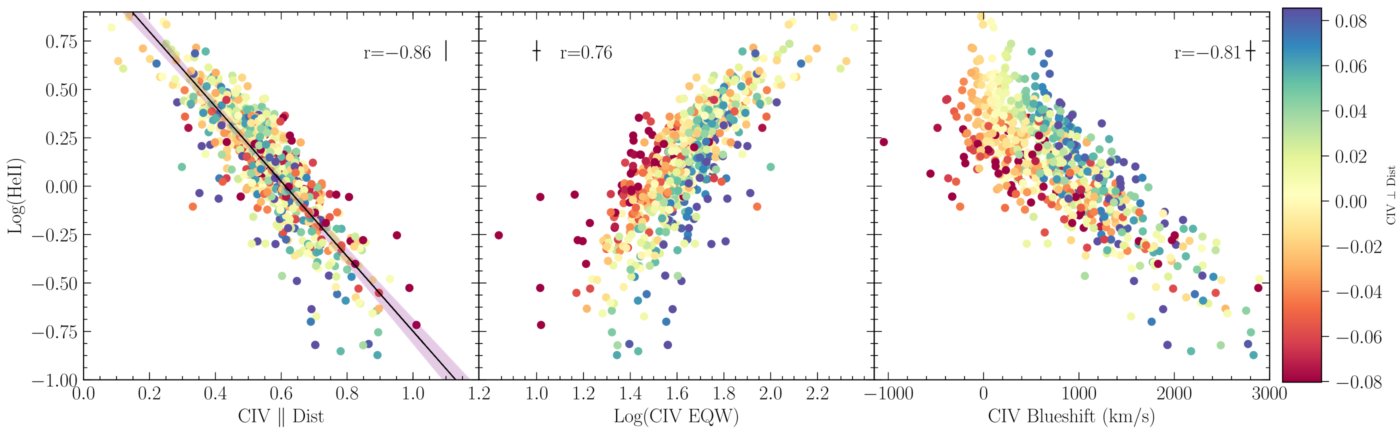

Figure 10. The C IV ∥ distance, log(C IV EQW), and C IV blueshift vs. log(He II EQW) for our sample colored by the C IV ⊥ distance shown in the left, middle, and right panels, respectively. The error bar for the C IV blueshift is the same as that from Figure 2; the error bars for the log(C IV EQW) and log(He II EQW) were carried out in a similar fashion, except in log space. The errors in C IV ∥ distance trace those of the underlying parameters, where the errors will be largest at the extreme where it is more difficult to accurately measure the component with small values. The Pearson r (assuming a linear correlation) values for each relationship are displayed in each panel. The break in the log(He II EQW)−log(C IV EQW) relationship shown in Figure C1 of Timlin et al. (2021b) is shown to be present at different C IV EQWs for different C IV ⊥ distances. Note that the linear trend with log(He II EQW) with the smallest scatter is that with the C IV ∥ distance. The linear best fit to the distribution is shown as the black solid line, with 3σ contours shown in light purple.

quasars at low C IV EQW can have both low and high C IV blueshift, and quasars at low C IV blueshift can have either low or high C IV EQW. In relation to taking spectral measurements, however, the C IV line is a much stronger emission line than He II, which is part of a complex at the edge of the C IV line and can be contaminated by iron (see Figure 2(b) of Laor et al. 1997, as well as Vestergaard & Wilkes 2001).

We gauge the utility of the C IV ∥ distance parameter in comparison to $\alpha_{\rm ox}$ and the He II EQW in order to determine whether it is an effective SED indicator when X-ray data and high-S/N UV spectra (for measuring He II EQW with sufficient accuracy) are not available. While $\alpha_{\rm ox}$ is not a similarly robust indicator of a quasar's ionizing SED to the He II EQW (Ferland et al. 2020, Figure 1), we would nevertheless expect a similar gradient of $\alpha_{\rm ox}$ in C IV space to what we see occur with the He II EQW; see Figure 9.

Examining various C IV properties versus He II EQW and versus $\alpha_{\rm ox}$ (see Appendix C) shows that there is always more scatter in the latter set of plots. This scatter may occur as a result of several factors. Generally, one would expect the He II EQW to be better correlated with C IV properties, as the cross section of outer shell electrons is higher to EUV photons than the X-ray. It is further possible that, despite the sensitive sample cut and the additional Γ–$\Delta\alpha_{\rm ox}$ cut implemented on our sample, the effects of variability and absorption (and/or orientation) result in a weaker correlation with $\alpha_{\rm ox}$ than He II.

Timlin et al. (2021b) found that it was necessary to adopt a double power law to fit the log(He II EQW)–log(C IV EQW) distribution, which we illustrate in the middle panel of Figure 10. We note that the nonlinearity is well characterized by the C IV ⊥ distance. That is, the nonlinearity seen by Timlin et al. (2021b) is exactly the nonlinearity that we attempt to correct by defining the C IV ∥ and C IV ⊥ distances instead of the EQW or blueshift alone, and the C IV ∥ distance might be the C IV parameter that correlates best with $L/L_{\rm Edd}$ (i.e., without a break). The left panel of Figure 10 demonstrates the utility of this approach, as it shows that the C IV ∥ distance and log(He II EQW) are more clearly linearly correlated. In addition, the C IV ∥ distance is shown to weakly anticorrelate with $\Delta\alpha_{\rm ox}$ (see Figure 11), indicating that the correlation with $\alpha_{\rm ox}$ (and thus also He II EQW) is not simply due to a dependency on L. Because it is not clear that the relationship between $\Delta\alpha_{\rm ox}$ and the C IV ∥ distance is linear, we here report a Spearman rank correlation coefficient r of −0.25 and a null p-value of 1.3e−12.

We find the following linear relation for the C IV ∥ distance and log(He II) EQW:

$$\begin{aligned} &\mathrm{Log(HeII\ EQW)} = (-1.9353 \pm 0.0411)\\ &\mathrm{C\,IV}\|\mathrm{Distance} + (1.1853 \pm 0.0237), \end{aligned} \tag{5}$$

with the intrinsic scatter on the relationship being $\sigma_i = 0.161$. Unlike the relationship between the He II EQW and C IV EQW found by Timlin et al. (2021b), there is no scatter shown by the C IV ⊥ distance in the relationship between the He II EQW and the C IV ∥ distance, most likely because both of the latter parameters account for the nonlinearity of the C IV parameter space. The relationship between the C IV ∥ distance and the log (He II EQW) has the strongest Pearson r value, −0.86, with greater significance in contrast to the C IV EQW and even the C IV blueshift, with r values of −0.81 and 0.76, respectively. The null p-values for all of these relationships are many orders of magnitude smaller than $p = 0.01$ and are essentially 0. We conclude that, in the case where the data quality is low and the He II EQW cannot be measured reliably, the C IV ∥ distance measurement can be used as a robust proxy. The C IV ∥ distance is a stronger indicator of the ionizing SED than $\alpha_{\rm ox}$, which could marginalize the need for X-ray data in some investigations.

4.4. SED/Geometry Changes across C IV Space

We seek to use these trends in He II versus C IV properties to understand the underlying physical parameters driving the changes in a quasar's ionization state. In the paradigm of Giustini & Proga (2019) both mass and accretion rate set the ionization state and the relative geometries of the components of the central engine (see their Figure 2). Specifically, the peak emission frequency and temperature for a local blackbody accretion disk model are proportional to $(l/M)^{\frac{1}{4}}$, with $l = L/L_{\rm Edd}$ (Laor & Davis 2011).

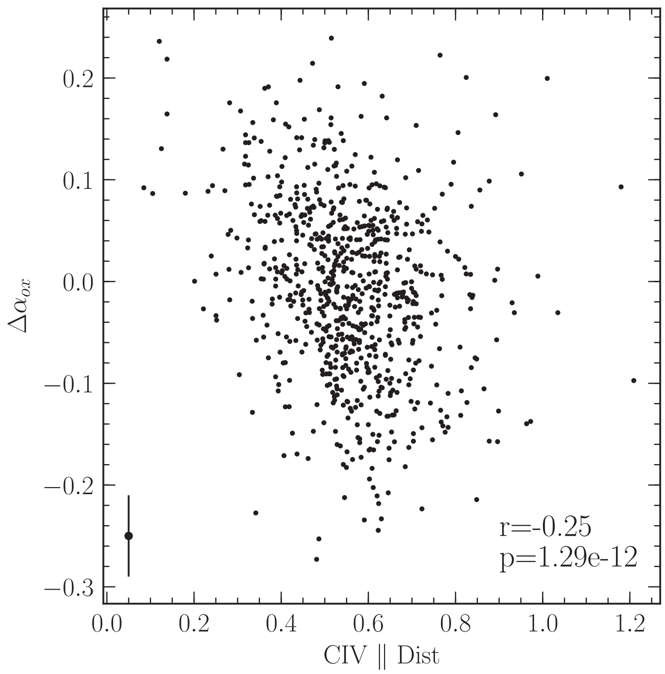

Figure 11. $\Delta\alpha_{\rm ox}$ vs. C IV || distance. Here we report a residual correlation between the two parameters, with a Spearman rank correlation coefficient r of -0.25 and a null p-value of 1.3e−12. This residual correlation indicates that the relationship between the C IV || distance and $\alpha_{\rm ox}$ is not simply due to luminosity. The error bar for $\Delta\alpha_{\rm ox}$ is the same as that given in Figure 7.

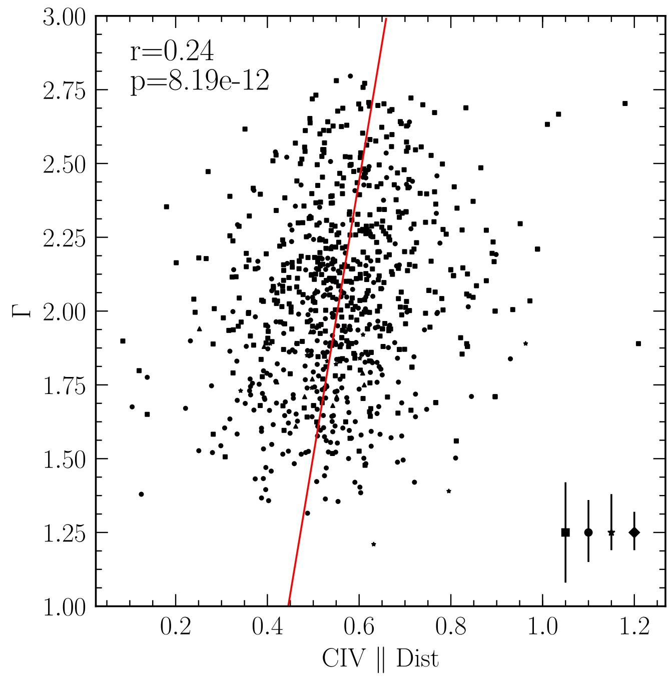

Figure 12. Γ vs. C IV || distance (with the latter parameter being approximated using HRs). Error bars and markers are the same as in Figure 7. A Pearson rank correlation test shows that a weak correlation between the two parameters exists, with an r value of 0.24 and a null p-value of 8.19e−12; however, this occurs only when examining our "Good" subsample.

The expectation that the C IV || distance might correlate with $L/L_{\rm Edd}$ arises from previous studies linking the traditional C IV parameters with $L/L_{\rm Edd}$. As discussed in Section 3.1, C IV EQW has been found to be strongly anticorrelated with $L/L_{\rm Edd}$ (except for some weak-lined quasars (WLQs); Shemmer & Lieber 2015). In relation to the C IV blueshift, the Giustini & Proga (2019) model would suggest that instead the main driver of change is black hole mass.

However, we find evidence that the C IV EQW does not simply anticorrelate with $L/L_{\rm Edd}$, nor C IV blueshift with black hole mass. In Rivera et al. (2020), it was established that, while accounting for continuum variability, quasars with high EQWs still exhibited changes in their EQW values even though their masses were not changing. These changes in C IV EQW lend support to the MBE description, as it would seem to indicate that changes in $L/L_{\rm Edd}$ are responsible for changes in the C IV EQW. It was also found that quasars with higher blueshifts exhibited changes in blueshift, again, while their masses were not changing. These changes in blueshift and EQW indicate that the direction of change in $L/L_{\rm Edd}$ is instead given by the best-fit curve (i.e., the C IV || distance) shown in Figure 2 rather than in the direction of either C IV parameter alone.

Figure 12 presents a related conundrum given that we have just argued that C IV || distance tracks $L/L_{\rm Edd}$ and that there is a long history of arguments that Γ similarly tracks $L/L_{\rm Edd}$; see Section 1. Yet Figure 12 (see also Appendix C) reveals only a weak correlation between the C IV || distance and Γ; a Pearson rank correlation gives an r value of 0.24 and a null p-value of 8.19e−12. Moreover, the trend only emerges when examining the "Good" sample. This lack of correlation could mean that one or both parameters are, in fact, not good tracers of $L/L_{\rm Edd}$. Indeed, Trakhtenbrot et al. (2017) have argued that Γ may not be a robust indicator of $L/L_{\rm Edd}$; thus, the lack of correlation is perhaps not surprising, and it would explain our finding in Figure 7 that C IV || distance and Γ are largely orthogonal. However, that figure may also reveal opportunities for further understanding the discrepancy if the data following the absorption/reddening tracks are indicative of the measured Γ not representing the intrinsic Γ. That said, applying an absorption correction would appear to make $\Delta\alpha_{\rm ox}$ a better indicator of $L/L_{\rm Edd}$ (if C IV || distance is the best tracer) than it would Γ. Either way, further investigations similar to Trakhtenbrot et al. (2017) are needed. For example, the relationship between the C IV || distance and $L/L_{\rm Edd}$ can be examined using Hβ calculated $L/L_{\rm Edd}$ values (Matthews et al. 2021) and high-quality C IV data from SDSS, and Γ can be tested against these $L/L_{\rm Edd}$ values as well using X-ray data with sufficiently high counts above rest frame 2 keV.

This result is interesting in terms of our hypothesis about how one might expect the model of Giustini & Proga (2019) to map to the C IV parameter space. Specifically, we might have expected that the width parameterized by the C IV ⊥ distance in the middle of the C IV || distance distribution would reflect objects with the same $L/L_{\rm Edd}$ (which does appear to be the case), but with different luminosities and black hole masses. That is, two objects with the same $L/L_{\rm Edd}$ could represent objects with (1) moderate accretion rate and high mass or (2) high accretion rate and low mass (given that these parameters are in the numerator and denominator of $L/L_{\rm Edd}$, respectively). If that were the case, then we might expect to see changes in the X-ray properties *across* the C IV distribution (that is, in the C IV ⊥ direction) as indicated by Giustini & Proga (2019). However, we do not find this to be the case. Thus, some other physical parameter must be controlling the width of the C IV distribution at intermediate C IV || distances, and we are unable to use the data presented herein to address the relative geometry of the accretion disk and corona in the way that we might have hoped and expected.

In Rivera et al. (2020) the C IV parameter space was investigated using a possible orientation indicator (zero-velocity associated absorption lines; see Weymann et al. 1979; Stone & Richards 2019); quasars possessing such features are argued to have more edge-on orientations (Richards et al. 2021) and were found to be spread without bias through the C IV parameter space, indicating that the C IV parameter space does not appear to be driven by orientation. A different parameter, such as metallicity, might be responsible for changes along that direction. Higher metallicity has the effect of cooling the gas and weakening the C IV line (Figure 5 of Baskin et al. 2014).

5. Conclusion

In our investigation we sought to collect the largest possible sample of high-quality UV and X-ray quasar data in order to investigate which empirical parameters and SED indicators have the highest potential of correlating linearly with $L/L_{\rm Edd}$. In particular, we defined two new parameters, the C IV $\|$ and C IV $\perp$ distances, in order to address the nonlinearity of C IV blueshift or C IV EQW with trends in physical parameters. In addition, we investigated whether X-ray properties could reveal changes in the accretion disk/corona geometry across the width of the C IV parameter space. In Sections 3.1, 4.3, and 4.4 and Figures 2 and 10 we find the following: (1) The He II EQW (a known SED indicator) can be approximated using the C IV $\|$ distance. (2) Because the C IV $\|$ distance incorporates information from both the C IV EQW and the C IV blueshift, it is the most likely C IV parameter to be linearly correlated with $L/L_{\rm Edd}$; however, there is only a weak correlation between the C IV $\|$ distance and Γ (though the latter was calculated using lower-quality data using HRs). Future work will require more black hole mass estimates from lines other than C IV to confirm that a relationship between the C IV $\|$ distance and $L/L_{\rm Edd}$ exists and to determine whether it is stronger or weaker than that found between Γ and $L/L_{\rm Edd}$ when Γ is measured from spectra with 100 counts above rest frame 2 keV. (3) The scatter in the He II EQW−C IV EQW and He II EQW−C IV blueshift relationships can be described by the C IV $\perp$ distance, which is not found to correlate with luminosity. Although the Giustini & Proga (2019) model predicts the X-ray to be a viable tool to distinguish between high-mass quasars with moderate accretion rates and low-mass quasars with high accretion rate (at the same C IV $\|$ distance), we do not find this to be the case. An exploration of the C IV $\perp$ distance with UV and X-ray properties reveals that there is not an obvious difference in the corona/disk/wind geometry across the width of the C IV parameter space and that the changes in C IV properties with C IV $\perp$ distance are not probed by the optical/UV and X-ray metrics investigated.

We find that $\alpha_{\rm ox}$ is not as clean of an indicator of the ionizing SED as the log(He II EQW), as $\alpha_{\rm ox}$ can be affected by both absorption and variability (Sections 3.4.3, 3.4.1, and 4.3, Figures 7, 4, and 9). We find that the UV variability of the SDSS-RM quasars translates to ∼0.08 in the calculation of $\alpha_{\rm ox}$ (Section 3.4.1, Figure 4) and that including an estimate of X-ray variability as given in Timlin et al. (2021b) can bring the error range as high as 0.19.

Finally, we investigated whether our approach could identify methods of reducing scatter in $\alpha_{\rm ox}$ due to both physics and variability in order to improve cosmology estimates using the Risaliti & Lusso (2015) method. Follow-up work is planned in investigating the feasibility of using a multilinear regression between the C IV $\|$ distance, Γ, and $\Delta\alpha_{\rm ox}$ to determine a correction for $\alpha_{\rm ox}$. It may also be possible to identify quasars affected by variability if their $\Delta\alpha_{\rm ox}$ and C IV $\|$ distances do not align properly (i.e., the object does not fall in the expected colored track in Figure 7).

We thank current and former Drexel undergraduate students Nick Giardetti, Anastasia Pierdomenico, Keziah Sheldon, and Robyn Smith for their contributions to this and closely related work. We thank Elisabeta Lusso and John Timlin for sharing their data. This work was based in part on observations made with the NASA/ESA Hubble Space Telescope, obtained at the Space Telescope Science Institute, which is operated by the Association of Universities for Research in Astronomy, Inc., under NASA contract NAS5-26555. These observations are associated with program No. 14135. Support for program No. 14135 was provided by NASA through a grant from the Space Telescope Science Institute, which is operated by the Association of Universities for Research in Astronomy, Inc., under NASA contract NAS5-26555. Support for this work was provided by the National Aeronautics and Space Administration through Chandra award Nos. G07-18110X and AR1-22010X issued by the Chandra X-ray Center, which is operated by the Smithsonian Astrophysical Observatory for and on behalf of the National Aeronautics Space Administration under contract NAS8-03060. This material is based in part on work supported by the National Science Foundation under grant No. 1908716. Funding for SDSS-III has been provided by the Alfred P. Sloan Foundation, the Participating Institutions, the National Science Foundation, and the US Department of Energy Office of Science. The SDSS-III website is http://www.sdss3.org/. S.C.G. thanks the Canadian Natural Science and Engineering Research Council for support.

Appendix A
HST Data Analysis

It is not practical to directly determine black hole masses for a large number of high-z quasars such as those investigated herein in the same way that we can at low z through the use of "reverberation mapping" (RM) techniques (e.g., Lira et al. 2018; Kaspi et al. 2021). Instead, it is necessary to develop "scaling relations" that are bootstrapped from low-z RM sources in order to estimate black hole masses at high redshift (e.g., Kaspi et al. 2000; Vestergaard & Peterson 2006; Bentz & Katz 2015). However, the finding that RM quasars have a bias against objects with strong winds (Richards et al. 2011; Shen 2013) means that there may be systematic errors in black hole mass estimates for quasars with strong winds (see, e.g., Du & Wang 2019).

Furthermore, if there is a luminosity threshold for winds in quasars (Veilleux et al. 2013; Zakamska & Greene 2014), then it is natural that the RM sample (being low redshift and thus tending toward lower luminosity) lacks wind-dominated sources. As we are looking to make connections between the accretion disk, the corona, and winds in this paper, it is important to understand the extent to which winds may be operating in lower-luminosity quasars.

Full consideration of winds in lower-luminosity sources is beyond the scope of this paper; however, we have a sample in hand that has been analyzed in a similar manner to those discussed already. Full analysis of this sample will appear in a future paper in the context of a broader analysis of HST archival spectroscopy covering the C IV emission line of local AGNs and quasars.

Obtaining a sample from a ground-based survey that is simultaneously "like the RM sample" and that covers the C IV emission line is not possible owing to the rest wavelength of C IV. The HST objects that we analyze herein are thus chosen to be (1) low luminosity, (2) low redshift, (3) covering C IV, but also (4) expected to include objects with strong winds based on their EV1 properties, specifically those possessing large R (Fe II) values (Sulentic et al. 2007; Marziani et al. 2018).

Our HST targets were drawn from the 105,809 spectroscopically confirmed quasars from the SDSS's Seventh Data Release (DR7) quasar catalog (Schneider et al. 2010). Targets were limited in redshift to $0.45 \leqslant z \leqslant 0.55$ so as to include coverage of Lyα and C III] in addition to C IV in the Space Telescope Imaging Spectrograph (STIS; Pritchard et al. 2022) spectra and both Mg II and Hβ/[O III] in the SDSS spectra. The target luminosity was constrained to $\log L_{2500} < 30.33$ erg s^{-1} to create a sample that serves as a bridge between the low-luminosity RM quasars and the other sources analyzed herein. Finally, targets were required to have Galactic $E(B-V) < 0.04$ and GALEX near-UV detections brighter than 18.5, as the GALEX near-UV bandpass nearly matches the STIS spectral coverage.

This selection process yielded 128 quasars, 8 of which are radio-loud. We down-sampled to 26 radio-quiet quasars with $i < 17.5$. Unlike the classical RM sample, these objects more fully probe the so-called "Eigenvector 1" (EV1) parameter space (e.g., Shen & Ho 2014), including the high-R(Fe II) population, which is thought to be indicative of high $L/L_{\rm Edd}$. Our hypothesis is that broader coverage of EV1 parameter space will lead to extended coverage of C IV parameter space and be more likely to reveal wind-dominated quasars at low redshift.

Each quasar was observed for a single orbit (≳54 minutes) with STIS/CCD and G230LB grating, covering $1680 < \lambda < 3060$ (observed; $1120 < \lambda < 2040$) at $z \sim 0.5$ with the $52'' \times 0\farcs2$ slit at position E1 with ∼2160 s of "on-target" exposure. We analyze the spectra output by the standard STIS pipeline procedures, using the latest calibration frames appropriate for these observations. The C IV measurements are extracted in the same manner as the rest of the data presented herein—after first reconstructing the spectra using the ICA components defined by Rankine et al. (2020).

Appendix B
Chandra Data Analysis

In addition to the HST data for the sample described above, we have Chandra data, from Chandra Cycle 18, for 25 of the same sources. Observations occurred between 2016 December and 2017 August. Targets were centered on the ACIS-S3 CCD chip, with no grating or filter. Details of the observations are compiled in Table B1. We primarily used Chandra Interactive Analysis of Observations (CIAO) version 4.9 to analyze our data (Fruscione et al. 2006). The level 2 event files from 2017 October were retrieved from the Chandra archive. We then sliced each image to an area of 100 × 100 pixels (0.67 arcmin^2). Counts were binned using the CIAO function "dmcopy" to produce four types of images: ultrasoft band (usb, 0.2–0.5keV), soft band (sb, 0.5–2keV), hard band (hb, 2–10 keV), and full band (fb, 0.2–10 keV). Counts were

Table B1
Chandra Observation Log

ObsID	SDSS ID	Obs Date	Live Time (s)	z	N_H	i	$E(B–V)$
19535	J002019.22−110609.2	2017 Jan 16	3502	0.492	2.89	17.440	0.034
19536	J082024.21+233450.4	2017 Feb 1	2952	0.471	4.02	17.335	0.04
19537	J082658.85+061142.6	2016 Dec 29	3432	0.496	2.68	17.403	0.022
19538	J083332.92+164411.0	2017 Oct 12	2950	0.460	3.60	17.268	0.029
19539	J083510.36+035901.1	2017 Jun 12	2952	0.492	3.29	17.386	0.028
19540	J085116.14+424328.8	2017 Jan 15	2949	0.482	2.56	17.427	0.026
19541	J091451.42+421957.0	2017 Jan 11	3505	0.549	1.46	17.407	0.017
19542	J093502.52+433110.6	2017 Jan 12	2891	0.457	1.40	15.952	0.019
19543	J100054.96+262242.4	2017 Mar 4	3501	0.506	2.68	17.543	0.026
19544	J103320.65+274024.2	2017 Feb 1	3506	0.536	1.87	17.428	0.026
19545	J111138.66+575030.0	2017 Aug 31	2983	0.465	0.71	17.361	0.01
19546	J111941.12+595108.7	2017 Aug 12	3535	0.489	0.73	17.329	0.01
19547	J112224.15+031802.6	2017 Jan 28	2946	0.475	4.16	17.453	0.04
19548	J112614.93+310146.6	2017 Jan 23	3497	0.495	1.76	17.527	0.017
19549	J113327.78+032719.1	2017 Jan 27	3429	0.525	2.74	17.542	0.023
19550	J113923.66+002301.6	2017 Jan 25	3449	0.472	3.14	17.139	0.02
19551	J123734.47+444731.7	2017 Mar 3	2949	0.461	1.51	17.405	0.019
19552	J125415.55+480850.6	2017 Apr 5	3046	0.503	1.12	17.354	0.01
19553	J131627.84+315825.7	2017 Jan 25	3429	0.464	1.11	17.438	0.009
19554	J134701.54+215401.1	2017 Mar 22	3504	0.502	1.63	17.487	0.02
19555	J140331.29+462804.8	2017 Apr 20	2951	0.459	1.26	17.223	0.01
19556	J145334.13+311401.4	2017 Jan 31	2982	0.465	1.47	17.300	0.016
19557	J152654.61+565512.3	2017 Feb 13	3497	0.482	1.42	17.395	0.015
19558	J155837.77+081345.8	2017 Jan 21	3430	0.517	3.68	17.520	0.04
19559	J234145.51−004640.5	2017 Jun 22	3430	0.525	3.67	17.495	0.03

Note. Column (1): Chandra Observation ID. Column (2): SDSS J2000 identifier. Column (3): date of observation. Column (4): live time (s), or the amount of time during which the CCD was observing the source. Column (5): redshift. Column (6): Galactic absorption column density in units of 10^{20} cm^{-2}. Column (7): i-band magnitudes from the DR7 quasar catalog. Column (8): $E(B-V)$ values for each quasar.

Table B2
Chandra X-Ray Results

SDSS ID (1)	fb (2)	sb (3)	hb (4)	HR (5)	Γ (6)	$f_{2\ \mathrm{kev}}$ (7)	f_{X} (8)
J002019.22−110609.2	$58.3^{+8.7}_{-7.6}$	$36.5^{+7.1}_{-36.5}$	$21.9^{+5.8}_{-4.6}$	$-0.27^{+0.08}_{-0.08}$	$1.61^{+0.18}_{-0.16}$	1.88	5.92
J082024.21+233450.4	$122.9^{+12.1}_{-11.1}$	$96.9^{+10.9}_{-9.8}$	$26.4^{+6.2}_{-5.1}$	$-0.45^{+0.06}_{-0.06}$	$2.07^{+0.16}_{-0.15}$	5.20	6.63
J082658.85+061142.6	$73.0^{+9.6}_{-8.5}$	$52.4^{+8.3}_{-7.2}$	$20.7^{+5.6}_{-4.5}$	$-0.34^{+0.07}_{-0.07}$	$1.77^{+0.18}_{-0.16}$	2.49	6.01
J083332.92+164411.0	$111.6^{+11.6}_{-10.5}$	$73.5^{+9.6}_{-8.6}$	$37.6^{+7.2}_{-6.1}$	$-0.30^{+0.06}_{-0.07}$	$1.79^{+0.16}_{-0.15}$	4.72	6.80
J083510.36+035901.1	$51.1^{+8.2}_{-7.1}$	$31.6^{+6.7}_{-5.6}$	$18.7^{+5.4}_{-4.3}$	$-0.27^{+0.08}_{-0.08}$	$1.68^{+0.18}_{-0.17}$	2.06	6.91
J085116.14+424328.8	$13.9^{+4.8}_{-3.7}$	$7.0^{+3.8}_{-2.6}$	$7.0^{+3.8}_{-2.6}$	$-0.24^{+0.09}_{-0.09}$	$1.56^{+0.31}_{-0.18}$	0.51	7.13
J091451.42+421957.0	$28.5^{+6.4}_{-5.3}$	$20.7^{+5.6}_{-4.5}$	$7.9^{+3.9}_{-2.7}$	$-0.32^{+0.08}_{-0.09}$	$1.71^{+0.20}_{-0.18}$	0.94	6.11
J093502.52+433110.6	$478.8^{+22.9}_{-21.9}$	$320.6^{+18.9}_{-17.9}$	$159.5^{+13.7}_{-12.6}$	$-0.33^{+0.04}_{-0.04}$	$1.74^{+0.09}_{-0.09}$	18.44	7.41
J100054.96+262242.4	$47.7^{+8.0}_{-6.9}$	$33.2^{+6.8}_{-5.7}$	$13.7^{+4.8}_{-3.6}$	$-0.32^{+0.08}_{-0.07}$	$1.75^{+0.19}_{-0.17}$	1.61	5.90
J103320.65+274024.2	$59.2^{+8.7}_{-7.7}$	$34.4^{+6.9}_{-5.8}$	$24.8^{+6.1}_{-4.9}$	$-0.23^{+0.08}_{-0.08}$	$1.53^{+0.17}_{-0.16}$	1.85	6.13
J111138.66+575030.0	$46.4^{+7.9}_{-6.8}$	$36.4^{+7.1}_{-6.0}$	$9.9^{+4.3}_{-3.1}$	$-0.37^{+0.07}_{-0.08}$	$1.90^{+0.18}_{-0.19}$	1.89	7.29
J111941.12+595108.7	$26.4^{+6.2}_{-5.1}$	$16.5^{+5.2}_{-4.0}$	$8.0^{+4.0}_{-2.8}$	$-0.30^{+0.08}_{-0.09}$	$1.70^{+0.20}_{-0.19}$	0.90	6.19
J112224.15+031802.6	$26.4^{+6.2}_{-5.1}$	$12.6^{+4.7}_{-3.5}$	$13.8^{+4.8}_{-3.7}$	$-0.21^{+0.08}_{-0.09}$	$1.53^{+0.19}_{-0.18}$	0.98	6.86
J112614.93+310146.6	$119.3^{+12.0}_{-10.9}$	$87.8^{+10.4}_{-9.4}$	$31.5^{+6.7}_{-5.6}$	$-0.38^{+0.06}_{-0.06}$	$1.88^{+0.15}_{-0.15}$	4.05	6.03
J113327.78+032719.1	$119.2^{+12.0}_{-10.9}$	$87.5^{+10.4}_{-9.3}$	$28.4^{+6.4}_{-5.3}$	$-0.38^{+0.06}_{-0.06}$	$1.94^{+0.16}_{-0.15}$	4.30	5.95
J113923.66+002301.6	$72.9^{+9.6}_{-8.5}$	$22.7^{+5.8}_{-4.7}$	$50.3^{+8.1}_{-7.1}$	$-0.01^{+0.07}_{-0.08}$	$1.08^{+0.15}_{-0.16}$	1.92	6.40
J123734.47+444731.7	$101.1^{+11.1}_{-10.0}$	$72.3^{+9.5}_{-8.5}$	$28.9^{+6.4}_{-5.3}$	$-0.35^{+0.07}_{-0.07}$	$1.83^{+0.16}_{-0.15}$	4.04	7.21
J125415.55+480850.6	$154.0^{+13.4}_{-12.4}$	$103.7^{+11.3}_{-10.2}$	$49.6^{+8.1}_{-7.1}$	$-0.32^{+0.06}_{-0.06}$	$1.76^{+0.14}_{-0.14}$	6.01	7.50
J131627.84+315825.7	4.0	<3.0	<9.4	$-0.24^{+0.09}_{-0.10}$	$1.52^{+0.22}_{-0.19}$	<0.12	<6.40
J134701.54+215401.1	$89.2^{+10.5}_{-9.4}$	$69.7^{+9.4}_{-8.3}$	$19.6^{+5.5}_{-4.4}$	$-0.41^{+0.06}_{-0.07}$	$1.93^{+0.19}_{-0.13}$	3.11	6.03
J140331.29+462804.8	$17.8^{+5.3}_{-4.2}$	$8.0^{+4.0}_{-2.8}$	$8.9^{+4.1}_{-2.9}$	$-0.23^{+0.09}_{-0.09}$	$1.53^{+0.21}_{-0.18}$	0.65	7.40
J145334.13+311401.4	$23.7^{+5.9}_{-4.8}$	$6.0^{+3.6}_{-2.4}$	$17.7^{+5.3}_{-4.2}$	$-0.13^{+0.09}_{-0.09}$	$1.30^{+0.19}_{-0.18}$	0.79	7.46
J152654.61+565512.3	$67.0^{9.2}_{-8.2}$	$44.6^{+7.7}_{-6.6}$	$22.5^{+5.8}_{-4.7}$	$-0.31^{+0.07}_{-0.07}$	$1.71^{+0.17}_{-0.16}$	2.19	6.14
J155837.77+081345.8	$54.2^{8.4}_{7.3}$	$30.6^{+6.6}_{-5.5}$	$23.6^{+5.9}_{-4.8}$	$-0.23^{+0.08}_{-0.08}$	$1.54^{+0.17}_{-0.17}$	1.77	5.96
J234145.51−004640.5	$58.9^{+8.7}_{-7.7}$	$29.6^{+6.5}_{-5.4}$	$28.4^{+6.4}_{-5.3}$	$-0.19^{+0.08}_{-0.08}$	$1.51^{+0.17}_{-0.16}$	1.96	5.98

Note. Column (1): SDSS J2000 identifier. Columns (2), (3), and (4): full-band (0.5–10 keV), soft-band (0.5–2 keV), and hard-band (2–10 keV) counts, respectively. Column (5): fractional difference HR (H – S)/(H + S) (6) Γ calculated from using HRs generated from the Park (2006) method and propagated using the method of Gallagher et al. (2006). Column (7): flux density at 2 keV (in units of 10^{-11} mJy). Column (8): soft flux (in units of 10^{-13} erg cm^{-2}s^{-1}). Note that 1σ errors are on Columns (2), (3), (4), (5), and (6). Errors on the counts were calculated using Equations (7) and (14) of Gehrels (1986).

measured visually in each band as a check for the values derived from the wavelet-based source detection algorithm WavDetect (Freeman et al. 2002). All of the objects had discrepancies between the two count values of less than 3%. WavDetect was called with two different detection thresholds: 10^{-6} (used for a blind search) and 10^{-3} (used for known sources). The upper limit was designated to check the lower limit and to allow for easier identification of usb counts as originating from the source. The wavelet radii ("scales") used were 1, 1.414, 2, 2.828, and 4 pixels. These results are given in Table B2; see also Marlar et al. (2022).

As the majority of this sample had observed full-band counts <100, we used the Bayesian Estimation of Hardness Ratio code (BEHR; Park et al. 2006) to obtain estimates of Γ. We used the fractional difference HR $\left(=\frac{\mathrm{H}-\mathrm{S}}{\mathrm{H}+\mathrm{S}}\right)$, where H is the number of hard (2–10 keV) counts and S is the number of soft (0.5–2keV) counts. We choose this HR because the simple ratio has a skewed probability distribution. This method is superior to the classical HR (H/S) because it can generate HRs even in the case of low (or no) counts in one of the two bands (H or S) and it is better able to calculate errors that take upper limits into account.

In order to derive Γ values from the HRs, we used the ARF and RMF files created by specextract to simulate instrument response in XSPEC (Arnaud 1996) using the Galactic-absorbed power-law model `phabs*pow`. Absorption was not included in this calculation of Γ. The model simulation was iterated with Γ varying from 0 to 3 in steps of 0.01. The values for the Galactic absorption and 1 keV normalization were kept constant. The latter value was set at 1 photon cm^{-2} s^{-1} keV^{-1}, as this parameter did not affect the value of the HR. The XSPEC command `rate` was used to calculate the count rate within the two bands of interest (0.5–2 keV and 2–10 keV for the soft and hard bands, respectively). We used these values to determine the best Γ that corresponded to a given HR (Gallagher et al. 2006). The model full-band count rate was normalized to the observed full-band count rate for the derivation of $N_{1\mathrm{keV}}$. We calculated the soft-band flux and the flux density at 2 keV ($f_{2\mathrm{keV}}$) using these Γ and $N_{1\mathrm{keV}}$ values. The HRs, Γ values, soft fluxes, and 2 keV ($f_{2\mathrm{keV}}$) values are given in Table B2.

Before calculating the observed values of α_{ox}, we first needed to calculate each quasar's luminosity at 2500 Å. We measured the continuum flux density from a continuum plus emission fit to the SDSS spectra of the Mg II line at 2800 Å and extrapolated that continuum to determine the flux density at 2500 Å assuming the same spectral slope $\alpha_{\mathrm{UV}} = -0.5$ for each quasar. We converted the $f_{2\mathrm{keV}}$ and $f_{2500\,\text{Å}}$ flux densities to luminosities using the cosmological parameters from Planck Collaboration et al. (2016). We additionally calculated the expected value of α_{ox} using Equation (2). Table B3 contains the α_{ox} values and $\Delta\alpha_{\mathrm{ox}}$ for our observed targets.

These HST/Chandra targets are included in our analysis and are distinguished in the interactive plots presented in Appendix C as "HST/Chandra."

Table B3
α_{ox} and Associated Values

SDSS ID (1)	L_{2keV} (2)	L_{2500} (3)	α_{ox} (4)	$\Delta\alpha_{ox}$ (5)	C IV EQW (6)	C IV Blueshift (7)	He II EQW (8)
J002019.22−110609.2	1.58E26	1.58E30	−1.58	−0.14	54.2	234	3.0
J082024.21+233450.4	4.71E26	2.09E30	−1.47	−0.01	52.8	635	2.5
J082658.85+061142.6	2.27E26	1.90E30	−1.56	−0.11	44.9	184	3.3
J083332.92+164411.0	3.65E26	1.96E30	−1.49	−0.03	27.7	511	1.5
J083510.36+035901.1	1.77E26	2.05E30	−1.61	−0.15	40.0	461	1.8
J085116.14+424328.8	4.04E25	1.97E30	−1.84	−0.38	44.4	840	1.3
J091451.42+421957.0	1.06E26	2.24E30	−1.71	−0.24	48.2	132	3.6
J093502.52+433110.6	1.38E27	9.40E30	−1.52	0.07	46.4	−397	1.5
J100054.96+262242.4	1.52E26	1.87E30	−1.62	−0.17	29.4	651	2.3
J103320.65+274024.2	1.82E26	2.19E30	−1.60	−0.14	41.2	389	2.1
J111138.66+575030.0	1.56E26	1.96E30	−1.63	−0.18	40.9	527	2.8
J111941.12+595108.7	7.26E25	1.99E30	−1.74	−0.29	39.2	674	2.5
J112224.15+031802.6	7.4E25	1.99E30	−1.74	−0.28	24.7	689	1.8
J112614.93+310146.6	3.85E26	1.75E30	−1.46	−0.02	69.3	213	3.5
J113327.78+032719.1	4.79E26	2.23E30	−1.47	−0.01	119.4	−6	6.8
J113923.66+002301.6	1.2E26	1.13E30	−1.53	−0.13	50.9	−64	1.8
J123734.47+444731.7	3.18E26	2.35E30	−1.54	−0.07	30.4	875	1.3
J125415.55+480850.6	5.63E26	2.24E30	−1.43	+0.03	62.5	445	3.1
J131627.84+315825.7	<8.71E24	1.68E30	<−2.07	<−0.62	39.3	383	2.8
J134701.54+215401.1	3.1E26	1.68E30	−1.50	−0.05	50.1	399	2.5
J140331.29+462804.8	4.51E25	1.85E30	−1.81	−0.36	69.4	54	5.3
J145334.13+311401.4	5.15E25	2.42E30	−1.82	−0.343	46.8	213	1.8
J152654.61+565512.3	1.82E26	1.80E30	−1.58	−0.14	42.6	658	2.8
J155837.77+081345.8	1.62E26	1.98E30	−1.61	−0.15	54.3	410	3.5
J234145.51−004640.5	1.83E26	2.23E30	−1.60	−0.14	53.8	405	2.0

Note. Column (1): SDSS J2000 identifier. Column (2): the luminosity at 2 keV in erg s^{-1}. Column (3): optical luminosity at 2500 Å in erg s^{-1}. Column (4): observed α_{ox}. Column (5): $\Delta\alpha_{ox}$. Column (6): rest-frame C IV EQW (Å). Column (7): C IV blueshift (km s^{-1}). Column (8): rest-frame He II EQW (Å).

Appendix C Bokeh Plots

Each of the 2D figures in the text (and/or panels therein) can be reproduced using the interactive plots available in the online version. The interactive plots allow the option to include/exclude different subsets of the data and to highlight different data ranges (at the expense of not including a color bar for a third dimension). The interactive plots are organized into four tabs: one each for plots showing `C IV Distance` (shown in Figure 13), `C IV Blueshift`, `log L2500`, and `MISC` as a function of other properties. Some of these plots are redundant, but they are provided to make it easy to see the parameter landscape from the perspective of each of these properties at once. The *x*-axes of the plots in the C IV blueshift panel are arranged so that the median blueshift (as an indicator of "windiness") increases to the right. The fourth tab includes other plots of interest that are not included in the themes of the first three tabs.

Figure 1 is replicated in the third row of the third column (one indexed) of the third tab (log L2500). Figures 2, 6, and 9 can be recreated using the second column of the first row of the `Blueshift` tab, but with axes reversed to highlight the importance of blueshifts in assessing winds. Figures 4 and 8 can be recreated with the central panel of the `log L2500` tab (again with axes reversed). Exploration of variants of Figure 7 can be achieved with the top left panel of the `MISC` tab. Finally, the individual panels of Figure 10 can be constructed from the top right panel of the `C IV Distance` tab, the bottom left panel of the `MISC` tab, and the top right panel of the `C IV Blueshift` tab.

We close with some highlights where using the interactive figures enable extending the results from the main text.

Our analysis includes 26 of the 30 sources investigated by Nardini et al. (2019) and Lusso et al. (2021). Seven of those objects are identified as outliers in one or more of the Γ, α_{ox}, $\Delta\alpha_{ox}$, $\Delta(g-i)$, or C IV $\perp$ distance parameters. The last two parameters are independent of any analysis by the Nardini et al. (2019) team. Using our data and methods, five of these sources are likely normal but absorbed quasars. We find that SDSS J111120.59+243740.8 is the most likely candidate for being intrinsically X-ray weak, as it has somewhat unusual C IV parameters and is only mildly reddened in the optical/UV and absorbed in the X-ray. SDSS J090508.88+305757.3 is a candidate X-ray-normal WLQ (Luo et al. 2015). SDSS J120144.36+011611.6 is the most likely to be X-ray absorbed, as it is below the dashed line in Figure 7.

Our HST/Chandra sources also include (indeed are dominated by) X-ray-weak or absorbed sources, which is somewhat unexpected (given the selection of bright, blue sources) but similar to Nardini et al. (2019). The sources most likely to be absorbed (as opposed to intrinsically X-ray weak), being below the dashed line in Figure 7, are SDSS J085116.14+424328.8, SDSS J112224.15+031802.6, SDSS J113923.66+002301.6, SDSS J131627.84+315825.7, SDSS J140331.29+462804.8, and SDSS J145334.13+311401.4. The small range in luminosity but large range in predicted L/L_{Edd} results in a large range of C IV (and other) parameters. These objects were selected in a way that should avoid bias against strong winds, but we do not see any evidence for strong winds in the sample (having average or below blueshifts for their EQWs)—completely consistent with their UV luminosities and a possible minimum threshold for strong winds (and/or luminosity dependence of the wind strength).

The SDSS-RM sample is clustered at relatively small C IV distance, with a large clump at high blueshift. Due to a lack of

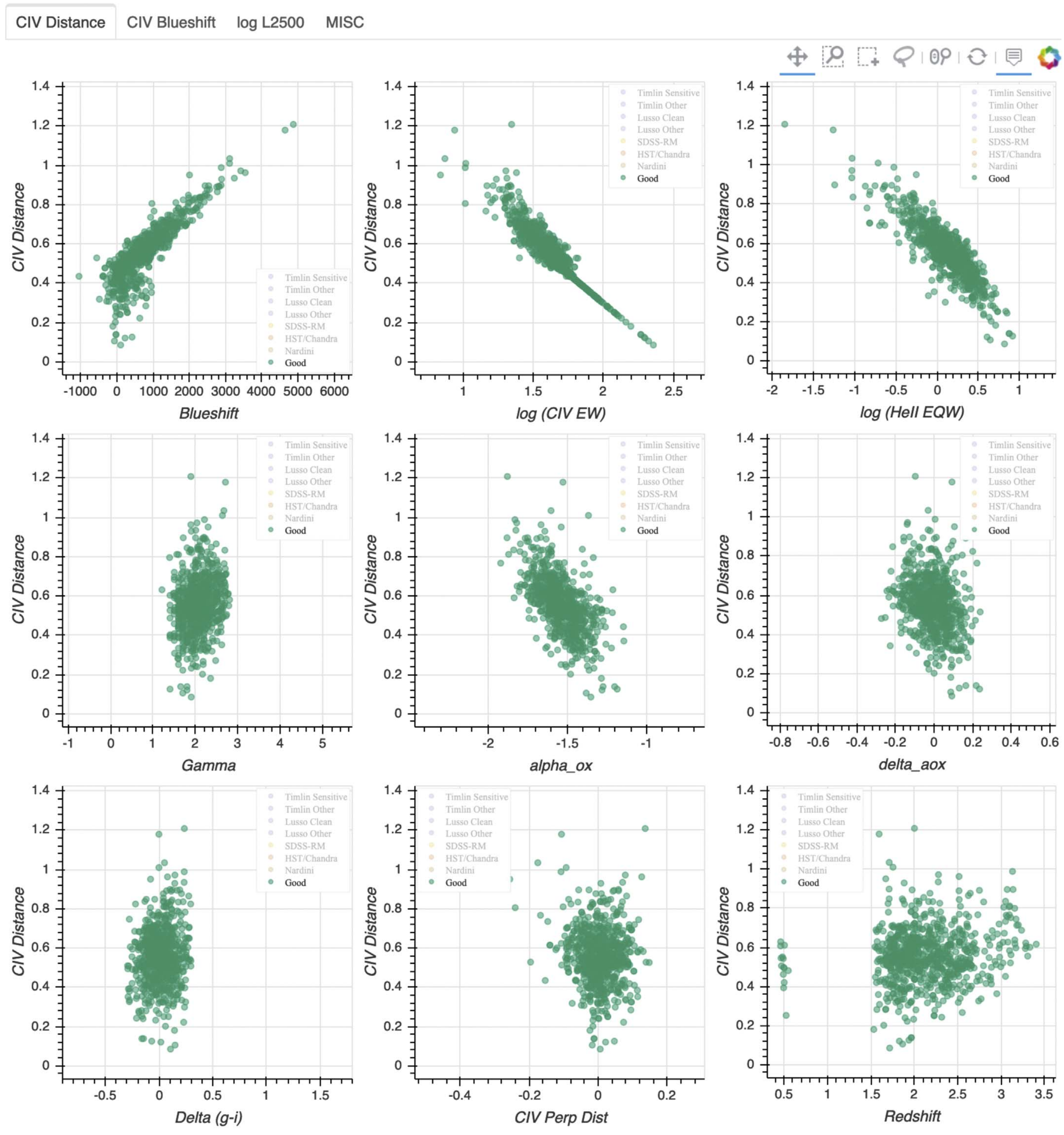

Figure 13. Relationship between C IV ∥ distance, blueshift, EQW, and other empirical properties of the quasars in the subsamples investigated herein. Included are He II EQW, Γ, $\alpha_{\rm ox}$, $\Delta\alpha_{\rm ox}$, $\Delta(g-i)$, the C IV perpendicular distance, and redshift. The online interactive figure allows users to see all the combinations of data and select different subsets. At the top right are buttons that control the interaction with the online figures. These include (in order) tools to pan into and out of each panel (selected by default), zoom within a box, select subsets in a box, select subsets using a "lasso," zoom using the scroll wheel, reset all the plots, and hover over a point to get more information. The hover tool is on by default and provides the SDSS ID and redshift for each object. The legends are also interactive. Clicking on a legend entry will toggle that data set on or off. All plots are initiated with only the "good" subsample (in green) as defined in Section 3.4.3. Data from Timlin et al. (2020a) and Lusso et al. (2020) (Section 2.1) are colored in purple. Data from the HST/Chandra, SDSS-RM, and Nardini et al. (2019) subsample are colored in orange, gold, and brown, respectively. Data points selected using the box or lasso tool are colored in pink (regardless of their parent sample). Only one panel at a time can be used for the select tool, and only data sets turned "on" in that panel will be selected (if turned on) in other panels.

(The data used to create this figure are available.)

dynamic range in luminosity as a result of probing only a limited area of sky, this sample is not as capable of determining trends as the larger-area samples. However, it does follow the basic trends of the full sample.

X-ray weakness is a requirement for radiatively driven winds; however, there appear to be two populations of X-ray-weak quasars. Figure 7 prompts an investigation into whether the objects with low Γ and $\Delta\alpha_{\rm ox}$ values are simply absorbed, or whether there are physical differences between those objects and those with more normal Γ and $\Delta\alpha_{\rm ox}$. Using the interactive plots to highlight only the quasars with $\Delta\alpha_{\rm ox} < -0.3$ reveals that these objects are only present below a C IV EQW of 100 Å, which is the limit below which quasars are (empirically) more likely to form accretion disk winds. Performing a cut in the Γ–$\Delta\alpha_{\rm ox}$ space will likely remove quasars that are truly intrinsically weak, which we could determine by their UV parameters; however, since we are primarily interested in examining bulk trends in the UV/X-ray parameter spaces, a more in-depth study of those objects is needed but is beyond the scope of this paper.

Using the selection tools to instead highlight objects with intermediate C IV $\|$ distance ($\approx$0.5) or He II EW ($\approx$0.2) does not reveal any obvious trends as discussed in the main text. That is, X-rays do not reveal differences in accretion disk versus corona geometry as the source of spread in intermediate C IV properties. We further find that the ability to determine the direction perpendicular to the main source of variance in C IV parameter space (as characterized by the C IV $\perp$ distance) is unrelated to dust reddening or the luminosity-corrected shape of the UV−X-ray SED. That is, the width of the C IV distribution is not simply due to reddening or $\Delta\alpha_{\rm ox}$. However, isolating small and large C IV $\|$ distance sources does reveal systematic differences in the $\Gamma - \Delta\alpha_{\rm ox}$ space that extends to both the Timlin and Lusso "Other" samples, which is the basis for our quasar cosmology discussion in Section 4.1.

Lastly, we note how the interactive tools can be used to illustrate the importance of spanning a large range in optical/UV luminosity and cleaning the sample of absorbed sources when determining the $L_{\rm UV} - \alpha_{\rm ox}$ relationship, as the scatter is large and can be particularly misleading for a small range of luminosity (e.g., when considering only the Lusso or Timlin samples alone, rather than together). Indeed, even these data do not span the dynamic range of samples designed to overcome this very problem (e.g., Steffen et al. 2006).

ORCID iDs

Angelica B. Rivera https://orcid.org/0000-0001-8125-1669
Gordon T. Richards https://orcid.org/0000-0002-1061-1804
Sarah C. Gallagher https://orcid.org/0000-0001-6217-8101
Trevor V. McCaffrey https://orcid.org/0000-0002-9321-9559
Amy L. Rankine https://orcid.org/0000-0002-2091-1966
Paul C. Hewett https://orcid.org/0000-0002-6528-1937
Ohad Shemmer https://orcid.org/0000-0003-4327-1460

References

Allen, J. T., Hewett, P. C., Richardson, C. T., Ferland, G. J., & Baldwin, J. A. 2013, MNRAS, 430, 3510
Arnaud, K. A. 1996, in ASP Conf. Ser. 101, Astronomical Data Analysis Software and Systems V, ed. G. H. Jacoby & J. Barnes (San Francisco, CA: ASP), 17
Baldwin, J. A. 1977, ApJ, 214, 679
Baskin, A., Laor, A., & Hamann, F. 2013, MNRAS, 432, 1525
Baskin, A., Laor, A., & Hamann, F. 2015, MNRAS, 449, 1593
Baskin, A., Laor, A., & Stern, J. 2014, MNRAS, 438, 604
Bentz, M. C., & Katz, S. 2015, PASP, 127, 67
Boroson, T. A., & Green, R. F. 1992, ApJS, 80, 109
Brightman, M., Silverman, J. D., Mainieri, V., et al. 2013, MNRAS, 433, 2485
Brotherton, M. S., & Francis, P. J. 1999, ASP Conf. Ser. 162, Quasars and Cosmology, ed. G. Ferland & J. Baldwin, (San Francisco, CA: ASP), 395, arXiv:astro-ph/9811088
Coatman, L., Hewett, P. C., Banerji, M., & Richards, G. T. 2016, MNRAS, 461, 647
Collin, S., Kawaguchi, T., Peterson, B. M., & Vestergaard, M. 2006, A&A, 456, 75
Constantin, A., Green, P., Aldcroft, T., et al. 2009, ApJ, 705, 1336
Czerny, B., & Hryniewicz, K. 2011, A&A, 525, L8
Dietrich, M., Hamann, F., Shields, J. C., et al. 2002, ApJ, 581, 912
Done, C., Davis, S. W., Jin, C., Blaes, O., & Ward, M. 2012, MNRAS, 420, 1848
Du, P., & Wang, J.-M. 2019, ApJ, 886, 42
Evans, I. N., Primini, F. A., Glotfelty, K. J., et al. 2010, ApJS, 189, 37
Ferland, G. J., Done, C., Jin, C., Landt, H., & Ward, M. J. 2020, MNRAS, 494, 5917
Francis, P. J., Hewett, P. C., Foltz, C. B., & Chaffee, F. H. 1992, ApJ, 398, 476
Freeman, P. E., Kashyap, V., Rosner, R., & Lamb, D. Q. 2002, ApJS, 138, 185
Fruscione, A., McDowell, J. C., Allen, G. E., et al. 2006, Proc. SPIE, 6270, 62701V
Gallagher, S. C., Brandt, W. N., Chartas, G., et al. 2006, ApJ, 644, 709
Gehrels, N. 1986, ApJ, 303, 336
George, I. M., Turner, T. J., Yaqoob, T., et al. 2000, ApJ, 531, 52
Gibson, R. R., Brandt, W. N., & Schneider, D. P. 2008, ApJ, 685, 773
Giustini, M., & Proga, D. 2019, A&A, 630, A94
Hewett, P. C., & Wild, V. 2010, MNRAS, 405, 2302
Jansen, F., Lumb, D., Altieri, B., et al. 2001, A&A, 365, L1
Kaspi, S., Brandt, W. N., Maoz, D., et al. 2021, ApJ, 915, 129
Kaspi, S., Smith, P. S., Netzer, H., et al. 2000, ApJ, 533, 631
Kelly, B. C. 2007, ApJ, 665, 1489
Krawczyk, C. M., Richards, G. T., Gallagher, S. C., et al. 2015, AJ, 149, 203
Kruczek, N. E., Richards, G. T., Gallagher, S. C., et al. 2011, AJ, 142, 130
Laor, A., & Davis, S. W. 2011, MNRAS, 417, 681
Laor, A., Jannuzi, B. T., Green, R. F., & Boroson, T. A. 1997, ApJ, 489, 656
Lira, P., Kaspi, S., Netzer, H., et al. 2018, ApJ, 865, 56
Liu, T., Merloni, A., Simm, T., et al. 2020, ApJS, 250, 32
Luo, B., Brandt, W. N., Hall, P. B., et al. 2015, ApJ, 805, 122
Lusso, E., Nardini, E., Bisogni, S., et al. 2021, A&A, 653, A158
Lusso, E., & Risaliti, G. 2016, ApJ, 819, 154
Lusso, E., Risaliti, G., Nardini, E., et al. 2020, A&A, 642, A150
Lyons, L. 1991, A Practical Guide to Data Analysis for Physical Science Students (Cambridge: Cambridge Univ. Press)
Margala, D., Kirkby, D., Dawson, K., et al. 2016, ApJ, 831, 157
Marlar, A., Shemmer, O., Brotherton, M. S., Richards, G. T., & Dix, C. 2022, ApJ, 931, 41
Marziani, P., Dultzin, D., Sulentic, J. W., et al. 2018, FrASS, 5, 6
Matthews, B. M., Shemmer, O., Dix, C., et al. 2021, ApJS, 252, 15
McCaffrey, T. V., & Richards, G. T. 2021, CIV_Distance doi:10.17918/CIVdistance
Miller, B. P., Brandt, W. N., Schneider, D. P., et al. 2011, ApJ, 726, 20
Mingo, B., Watson, M. G., Rosen, S. R., et al. 2016, MNRAS, 462, 2631
Murray, N., Chiang, J., Grossman, S. A., & Voit, G. M. 1995, ApJ, 451, 498
Nardini, E., Lusso, E., Risaliti, G., et al. 2019, A&A, 632, A109
Pâris, I., Petitjean, P., Aubourg, É., et al. 2012, A&A, 548, A66
Pâris, I., Petitjean, P., Aubourg, É., et al. 2014, A&A, 563, A54
Park, T., Kashyap, V. L., Siemiginowska, A., et al. 2006, ApJ, 652, 610
Pedregosa, F., Varoquaux, G., Gramfort, A., et al. 2011, JMLR, 12, 2825
Phillips, M. M. 1993, ApJL, 413, L105
Planck Collaboration, Ade, P. A. R., Aghanim, N., et al. 2016, A&A, 594, A13
Pritchard, L., Welty, D., Jones, A., et al. 2022, STIS Instrument Handbook, v.21.0 (Baltimore, MD: STScI)
Pu, X., Luo, B., Brandt, W. N., et al. 2020, ApJ, 900, 141
Rankine, A. L., Hewett, P. C., Banerji, M., & Richards, G. T. 2020, MNRAS, 492, 4553
Reeves, J. N., & Turner, M. J. L. 2000, MNRAS, 316, 234
Richards, G. T., Hall, P. B., Vanden Berk, D. E., et al. 2003, AJ, 126, 1131
Richards, G. T., Kruczek, N. E., Gallagher, S. C., et al. 2011, AJ, 141, 167
Richards, G. T., Lacy, M., Storrie-Lombardi, L. J., et al. 2006, ApJS, 166, 470
Richards, G. T., Plotkin, R. M., Hewett, P. C., et al. 2021, ApJL, 914, L14
Risaliti, G., & Lusso, E. 2015, ApJ, 815, 33
Risaliti, G., Young, M., & Elvis, M. 2009, ApJL, 700, L6
Rivera, A. B., Richards, G. T., Hewett, P. C., & Rankine, A. L. 2020, ApJ, 899, 96

Schneider, D. P., Richards, G. T., Hall, P. B., et al. 2010, VizieR Online Data Catalog: The SDSS-DR7 quasar catalog
Shemmer, O., Brandt, W. N., Netzer, H., Maiolino, R., & Kaspi, S. 2008, ApJ, 682, 81
Shemmer, O., Brandt, W. N., Schneider, D. P., et al. 2006, ApJ, 644, 86
Shemmer, O., & Lieber, S. 2015, ApJ, 805, 124
Shen, Y. 2013, BASI, 41, 61
Shen, Y., Brandt, W. N., Dawson, K. S., et al. 2015, ApJS, 216, 4
Shen, Y., & Ho, L. C. 2014, Natur, 513, 210
Shen, Y., Richards, G. T., Strauss, M. A., et al. 2011, ApJS, 194, 45
Steffen, A. T., Strateva, I., Brandt, W. N., et al. 2006, AJ, 131, 2826
Stone, R. B., & Richards, G. T. 2019, MNRAS, 488, 5916
Sulentic, J. W., Bachev, R., Marziani, P., Negrete, C. A., & Dultzin, D. 2007, ApJ, 666, 757
Tananbaum, H., Avni, Y., Branduardi, G., et al. 1979, ApJL, 234, L9
Timlin, J., Zhu, S., Brandt, W. N., & Laor, A. 2021a, RNAAS, 5, 101
Timlin, J. D., Brandt, W. N., & Laor, A. 2021b, MNRAS, 504, 5556
Timlin, J. D., Brandt, W. N., Ni, Q., et al. 2020a, MNRAS, 492, 719
Timlin, J. D. I., Brandt, W. N., Zhu, S., et al. 2020b, MNRAS, 498, 4033
Trakhtenbrot, B., Ricci, C., Koss, M. J., et al. 2017, MNRAS, 470, 800
Veilleux, S., Meléndez, M., Sturm, E., et al. 2013, ApJ, 776, 27
Vestergaard, M., & Peterson, B. M. 2006, ApJ, 641, 689
Vestergaard, M., & Wilkes, B. J. 2001, ApJS, 134, 1
Wang, H., Wang, T., Zhou, H., et al. 2011, ApJ, 738, 85
Webb, N. A., Coriat, M., Traulsen, I., et al. 2020, A&A, 641, A136
Weymann, R. J., Morris, S. L., Foltz, C. B., & Hewett, P. C. 1991, ApJ, 373, 23
Weymann, R. J., Williams, R. E., Peterson, B. M., & Turnshek, D. A. 1979, ApJ, 234, 33
Yip, C. W., Connolly, A. J., Vanden Berk, D. E., et al. 2004, AJ, 128, 2603
York, D. G., Adelman, J., Anderson, J. E. J., et al. 2000, AJ, 120, 1579
Zakamska, N. L., & Greene, J. E. 2014, MNRAS, 442, 784